Cell Systems

Article

Temperature Sensing Is Distributed throughout the Regulatory Network that Controls *FLC* Epigenetic Silencing in Vernalization

Graphical Abstract

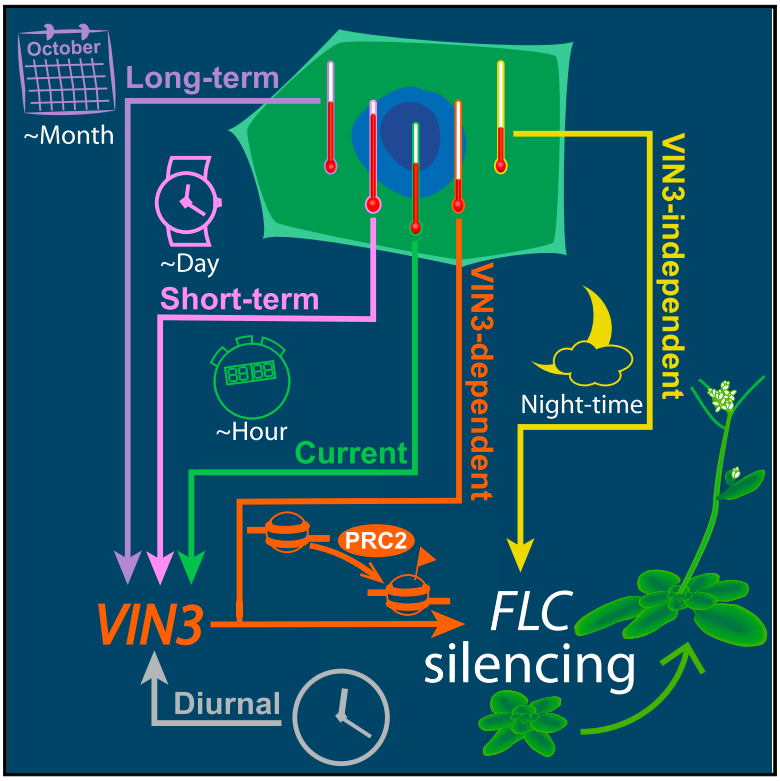

Highlights

- Multiple thermosensory inputs with distinct timescales regulate vernalization
- One input identified as a short-term memory of warm temperature spikes
- Predictive mathematical model of vernalization in controlled and field conditions
- Model predicts future responses to increasingly warm and fluctuating climates

Authors

Rea L. Antoniou-Kourounioti, Jo Hepworth, Amélie Heckmann, ..., Svante Holm, Caroline Dean, Martin Howard

Correspondence

caroline.dean@jic.ac.uk (C.D.), martin.howard@jic.ac.uk (M.H.)

In Brief

We investigate temperature sensing in the *Arabidopsis thaliana* vernalization pathway, responsible for accelerated flowering after winter. We uncover multiple thermosensory inputs, each sensing a distinct feature of the temperature signal with a distinct timescale. Such sensing allows the plant to recognize winter cold in a complex and variable environment. We develop a predictive mathematical model for vernalization and find that two predicted features of future climates, higher mean temperatures and larger temperature fluctuations, will both affect the rate of vernalization.

Antoniou-Kourounioti et al., 2018, Cell Systems 7, 643–655
December 26, 2018
https://doi.org/10.1016/j.cels.2018.10.011

CellPress

Cell Systems
Article

Temperature Sensing Is Distributed throughout the Regulatory Network that Controls *FLC* Epigenetic Silencing in Vernalization

Rea L. Antoniou-Kourounioti,[1,4] Jo Hepworth,[1,4] Amélie Heckmann,[1] Susan Duncan,[1] Julia Qüesta,[1] Stefanie Rosa,[1] Torbjörn Säll,[2] Svante Holm,[3] Caroline Dean,[1,*] and Martin Howard[1,5,*]
[1]John Innes Centre, Norwich Research Park, Norwich NR4 7UH, UK
[2]Department of Biology, Lund University, Lund 223 62, Sweden
[3]Department of Natural Sciences, Mid Sweden University, Sundsvall 851 70, Sweden
[4]These authors contributed equally
[5]Lead Contact
*Correspondence: caroline.dean@jic.ac.uk (C.D.), martin.howard@jic.ac.uk (M.H.)
https://doi.org/10.1016/j.cels.2018.10.011

SUMMARY

Many organisms need to respond to complex, noisy environmental signals for developmental decision making. Here, we dissect how *Arabidopsis* plants integrate widely fluctuating field temperatures over month-long timescales to progressively upregulate *VERNALIZATION INSENSITIVE3 (VIN3)* and silence *FLOWERING LOCUS C (FLC)*, aligning flowering with spring. We develop a mathematical model for vernalization that operates on multiple timescales—long term (month), short term (day), and current (hour)—and is constrained by experimental data. Our analysis demonstrates that temperature sensing is not localized to specific nodes within the *FLC* network. Instead, temperature sensing is broadly distributed, with each thermosensory process responding to specific features of the plants' history of exposure to warm and cold. The model accurately predicts *FLC* silencing in new field data, allowing us to forecast *FLC* expression in changing climates. We suggest that distributed thermosensing may be a general property of thermoresponsive regulatory networks in complex natural environments.

INTRODUCTION

Alignment of plant development to favorable environmental conditions requires mechanisms for sensing and integrating the environmental cues that indicate seasonal change. One of the key seasonal indicators is temperature, and many plant species need to experience winter chilling in order to flower (Andrés and Coupland, 2012; Shrestha et al., 2014). In the Brassicaceae family, including *Arabidopsis thaliana*, the transcriptional regulator *FLOWERING LOCUS C* (*FLC*) represses the transition to flowering (Aikawa et al., 2010; Irwin et al., 2016; Kemi et al., 2013; Kiefer et al., 2017; Michaels and Amasino, 1999; Sheldon et al., 1999; Wang et al., 2009). *FLC* is downregulated by prolonged cold and epigenetically silenced to maintain this state into the spring to allow the plant to be maximally responsive to floral-promoting long-day photoperiods (reviewed in Bloomer and Dean [2017]). To accomplish this objective, the regulatory network controlling *FLC* must distinguish a clear seasonal signal over months, despite daily temperature fluctuations that can exceed average seasonal differences.

Previous work has shown that *FLC* downregulation during the cold is the result of at least two separate thermosensory pathways. The first pathway acts to downregulate *FLC* transcription and is responsive to transient low temperatures, such as autumn cold (Hepworth et al., 2018; Swiezewski et al., 2009). The second pathway enacts epigenetic silencing of *FLC* and requires the action of the conserved Polycomb Repressive Complex 2 (PRC2) combined with members of a PHD protein family, including VERNALIZATION INSENSITIVE3 (VIN3; De Lucia et al., 2008; Sung and Amasino, 2004). *VIN3* is a key thermosensory component of the vernalization response, with *VIN3* mRNA levels slowly rising with increasing weeks of cold exposure but rapidly decreasing in the warm (Bond et al., 2009a; De Lucia et al., 2008; Finnegan et al., 2011; Sung and Amasino, 2004). These dynamics are consistent with control of *VIN3* itself by (at least) two upstream thermosensitive inputs. *VIN3* expression is very sensitive to spikes of warm temperature during the day, and so epigenetic silencing only occurs once winter temperatures prevail (Hepworth et al., 2018).

Investigation of such a complex phenomenon requires interdisciplinary approaches, exploiting mathematical modeling as well as experiments (Aikawa et al., 2010; Chew et al., 2012; Kudoh, 2016; Satake et al., 2013; Wilczek et al., 2009). This approach has been used to forecast flowering responses (Aikawa et al., 2010; Chew et al., 2012; Satake et al., 2013). However, it is unclear how *VIN3* and *FLC* expression are controlled by a plant's history of warm and cold exposure (Finnegan et al., 2011; Hepworth et al., 2018; Kim et al., 2010; Wollenberg and Amasino, 2012). Here, we systematically investigate the temperature dependencies for *VIN3* and *FLC* dynamics, using a repeated cycle of hypothesis generation via mathematical modeling, followed by experiments under both controlled and natural field conditions (see Figure S1A). This methodology identifies multiple thermosensing inputs into both *VIN3* and *FLC*

expression that respond to distinct features of the fluctuating temperature profile. The resulting mathematical model also successfully predicts *VIN3*/*FLC* expression dynamics for newly acquired field measurements. More broadly, our data, with numerous temperature-dependent steps for *VIN3*/*FLC*, support the general hypothesis that temperature sensitivity will be distributed throughout thermally responsive regulatory networks in biological systems, rather than being concentrated at particular steps with the rest of the network being temperature compensated. We emphasize that this distributed property of temperature sensing does not refer to a spatial distribution but rather to the distribution of the temperature response over many nodes of the network that regulates *VIN3*/*FLC*, a feature which is likely to be a general property of temperature sensing in biology. Overall, this work greatly extends our ability to understand and predict the thermal responses of biological systems to complex, real-world environmental conditions.

RESULTS

Initial Mathematical Model for Temperature-Sensitive *VIN3* Dynamics

In order to fully understand how noisy field temperatures are integrated at *FLC*, we investigated the nature of the temperature inputs to the expression of the epigenetic regulator, *VIN3*. *VIN3* expression is influenced by at least two separate thermosensitive processes (Hepworth et al., 2018). One promotes expression while in the cold, providing the memory of cold duration with a long timescale of weeks, while a second reduces expression in the warm, with a fast-acting timescale of hours. The molecular basis of these processes is currently unknown but could include, for example, temperature-sensitive accumulation, depletion, conformational changes, or altered covalent modifications to proteins, RNA, or chromatin.

To investigate the properties of these thermosensitive processes without knowledge of their biophysical identities, we developed a mathematical model of *VIN3* dynamics. We were primarily constrained by the two very different timescales of the *VIN3* response. We proceeded by fitting the temperature dependencies in the model at each timescale based on our and others' previous experimental work (Bond et al., 2009a; De Lucia et al., 2008; Duncan et al., 2015; Finnegan et al., 2011; Greb et al., 2007; Hepworth et al., 2018; Sung and Amasino, 2004; Wollenberg and Amasino, 2012; Yang et al., 2017).

One temperature-sensitive pathway holds the memory of the duration of the cold. We termed this long term (*L*). For *L* to hold stable quantitative memory, an attractive hypothesis is a digital system similar to the one employed by *FLC* regulation (Angel et al., 2011, 2015; Berry et al., 2015), in which individual cells show bimodal expression of *FLC* (either some or none). However, single molecule RNA fluorescence *in situ* hybridization (FISH) (Figure S1B) clearly showed an analog increase in the *VIN3* RNA levels distributed evenly across different cells (Figures S1C–S1E). Hence, the effect of this thermosensitive process is graded, rather than all or nothing, at the level of *VIN3* RNA.

To produce the long-term, graded accumulation shown experimentally in Figures S1B–S1E, *L* must have a very slow degradation timescale (weeks) in the cold (defined here as less than approximately 15°C; Duncan et al., 2015; Hepworth et al., 2018; Wollenberg and Amasino, 2012). We previously showed that the long-term thermosensitive process is able to accumulate in conditions where the temperature fluctuates above 20°C for 4 hr daily (Hepworth et al., 2018). Therefore, the decay rate of *L* must also be relatively slow in warm temperatures, on a timescale of more than a few hours.

We modeled *L* such that it is produced only in the cold and degrades very slowly in both the cold and the warm, thereby integrating over the period of cold that the plant has experienced. To test this property, plants were grown in warm conditions for different lengths of time. When these plants were transferred to the cold for 1 day, they showed no evidence of increased *L*, since very low levels of *VIN3* expression were observed regardless of the duration of the growth time (Figure S1F). *L* does not, therefore, accumulate at high (~20°C) temperatures.

The second thermosensitive pathway, which here we term current (*C*), measures current temperature and has fast-acting dynamics. *C* is responsible for the rapid reduction in *VIN3* levels observed at high temperatures (Bond et al., 2009a; Finnegan et al., 2011; Greb et al., 2007; Hepworth et al., 2018; Sung and Amasino, 2004; Yang et al., 2017), so that it can reproduce the "absence of warm" response seen in Hepworth et al. (2018). However, there is also a graded response to cold in an intermediate temperature range, taking higher values at lower temperatures (Duncan et al., 2015; Hepworth et al., 2018; Wollenberg and Amasino, 2012). For simplicity, we modeled both these behaviors here as part of *C* (Figure S2A, equation for *C*), such that above this intermediate temperature range, it has a very low value, regardless of the temperature, and below this range, it takes its maximal value.

Additionally, transcription of *VIN3* is regulated by the circadian clock, with a peak of transcription in the afternoon in constant temperature conditions (Hepworth et al., 2018). For this aspect, we require an additional component of *VIN3* regulation, which we term diurnal (*D*), which we assume within this model to be temperature independent. We use a simplified function to represent the circadian clock (Figure S2A) as a mechanistic representation of this complex system is beyond the scope of this study and has been investigated in detail elsewhere (Locke et al., 2006; Sanchez and Kay, 2016). Both *C* and *D* must act directly on *VIN3* rather than on *L* due to the very different timescales of *C* and *D* (fast) as compared to *L* (slow) (Hepworth et al., 2018).

In principle, these pathways could act on *VIN3* transcription initiation, splicing, or degradation. However, we previously found similar expression patterns for both spliced and unspliced *VIN3* RNA (Hepworth et al., 2018). To explain this result, if splicing and degradation were modulated, these two processes would need to be altered in exactly the same way in response to temperature. In addition, the degradation rate of *VIN3* mRNA is observed to be fast in both the warm and the cold, with an estimated timescale of hours (Finnegan et al., 2011; Greb et al., 2007; Hepworth et al., 2018; Sung and Amasino, 2004), arguing against temperature regulation of degradation. In the model, we therefore assume the simpler hypothesis that only transcription initiation is altered by temperature, which naturally generates the same response for both spliced and unspliced *VIN3* levels.

We combined these observations to generate a simple ordinary differential equation model for temperature-dependent *VIN3* expression (Figure S2A). The three pathways operate

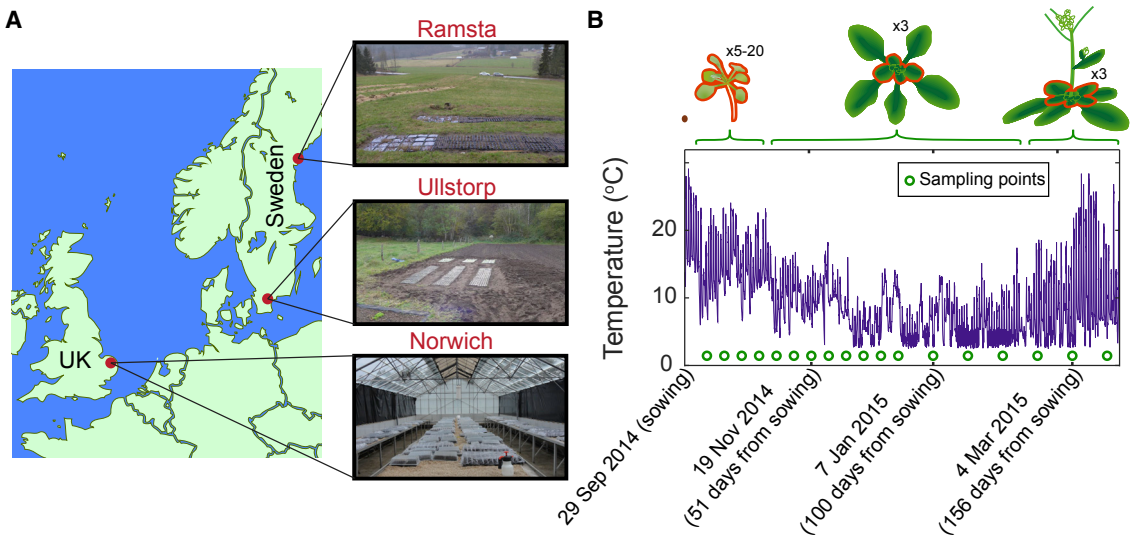

Figure 1. Experimental Method for Field Experiments

(A) Field sites in North Sweden (Ramsta), South Sweden (Ullstorp), and UK (Norwich). At the Swedish sites, plants were grown in trays bedded in the soil in the field. In Norwich, the plants were grown inside an unlit, unheated greenhouse with air-inlets, in trays bedded in vermiculite, ensuring the containment of transgenic lines while the plants still experienced natural conditions.

(B) Example of sowing and sampling setup in the field experiments, showing the Norwich site 2014–2015. The temperature profile is shown together with the dates of sampling. Above the temperature plot, the approximate plant size throughout the experiment is shown, together with the tissues that were collected in the samples depending on the plants' size (outlined in red), and the number of plants collected for each replicate. In Norwich, when plants were larger, only the youngest tissues were harvested, as indicated. 6 replicate samples were taken per time point, though some were lost in processing or unusable due to environmental factors, e.g., mudslides.

See also Table S6.

such that the rate of "production" of *VIN3* in the model is proportional to the product of *L*, *C*, and *D* (STAR Methods). This model was fitted to previously published data from controlled conditions (Hepworth et al., 2018). We found that the data could in all cases be successfully described by the *LCD* model (Figures S2B–S2G). To further test our understanding, we then designed further experiments and tried to interpret the results using this model, as described in the next section.

Additional Short-Term Memory of Absence of Warm Is Needed to Explain *VIN3* Dynamics

To understand temperature sensing in natural conditions, we carried out experiments in field sites in three different climatic locations: North Sweden field (two plantings, 2 weeks apart), South Sweden field, and an unheated, unlit greenhouse in Norwich, UK (Figure 1A; Hepworth et al., 2018). We sampled plants at regular intervals (Figure 1B), giving a high-resolution time series dataset for *FLC* and *VIN3* RNA (Hepworth et al., 2018). In field experiments, temperatures often spiked to high levels during the day in the autumn (Figure 1B), while, at the same time, the plants showed low *VIN3* levels, despite low average temperatures (Hepworth et al., 2018). High *VIN3* levels instead occurred later in the season when high temperature spikes were absent.

We dissected this absence of warmth response by testing if a short spike of high temperature, applied daily in controlled conditions, would be sufficient to reproduce this behavior. We used a spike of 2 hr since we had observed that, post-cold, in constant warm conditions (above 20°C), *VIN3* levels were significantly reduced after this time period (Hepworth et al., 2018). We additionally tested whether the spike would produce different responses if it was received during the day or night. We therefore designed conditions in which plants remained at constant 12°C except for 2 hr at 21°C, with the spike in temperature during the day (midday spike, 2 hr after dawn) when *VIN3* levels were high, but also during the night (night spike, 6 hr after dusk) when *VIN3* levels were low (Figure 2A). We compared these conditions with constant 12°C, as well as with the constant and fluctuating temperature conditions (both with average 14.2°C) used previously (Hepworth et al., 2018).

We found that 2 hr of warm temperatures were sufficient to reduce *VIN3* expression levels, as expected given the known fast response of *VIN3* to warmth (Figures 2A–2C, midday spike versus constant 12°C). However, the timing of the temperature spike was not important for its effect on expression: the night spike had a similar effect on the following day's *VIN3* profile as a midday spike during the day of sampling (Figures 2A–2C, night spike versus midday spike). Immediate temperature sensing (*C*) is insufficient to explain this phenomenon, as the night spike occurred 10 hr before *VIN3* reduction is greatest. Potentially, the temperature spikes could have caused a reduction in the long-term response. However, the influence of the spikes did not continue for longer than 24 hr: when plants were moved from 4 weeks in spike conditions back to constant 12°C, these plants behaved similarly to those with 12°C constant treatment without spikes (Figures 2A–2C, spike memory versus constant 12°C), indicating that *L* is unaltered.

It is important to note that, in our reasoning above, although we referred to *L* and *C*, we did not use any of the specific

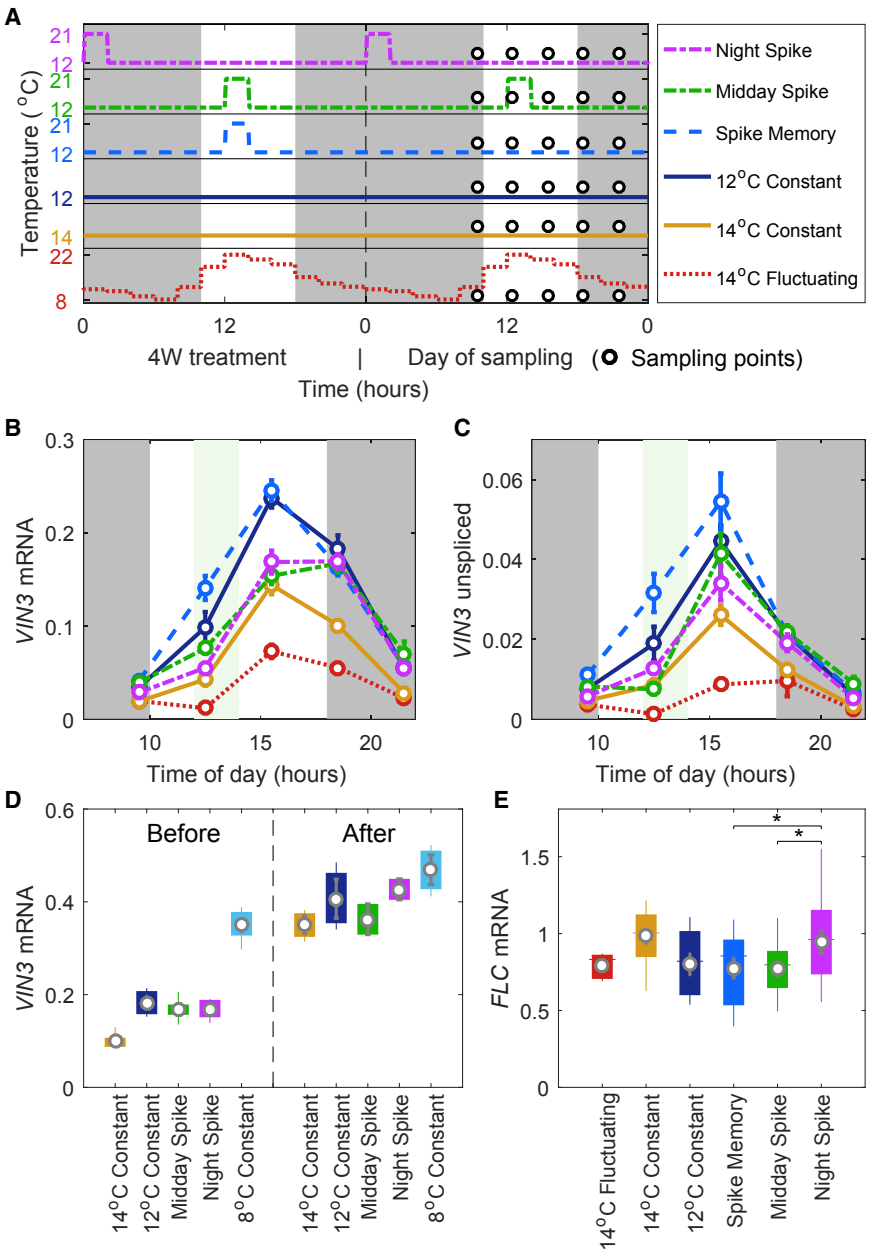

Figure 2. Short Duration Spikes to High Temperature Affect *VIN3* Expression

(A) Temperature conditions given daily for 4 weeks (left) and then on day of sampling (right). Plants were grown in 20°C (night) or 22°C (day) 16-hr photoperiod for 1 week and then transferred to the conditions shown on the left. Dark background indicates nighttime (8-hr photoperiod).

(B) *VIN3* spliced expression during the day of sampling, sampled every 3 hr over a 12-hr period as shown. The green background indicates the time of the high temperature spike in the midday spike conditions. n = 1–9; average > 6.

(C) *VIN3* unspliced expression from experiment in (B). n = 1–9; average > 6.

(D) *VIN3* expression after 4 weeks cold in indicated conditions. "Before" refers to samples taken at 18:30 on sampling day, in the conditions indicated. "After" refers to samples that after 4 weeks cold in indicated conditions were further treated with, first, a further 4 days in the conditions indicated and then transferred in the afternoon (before dark) to constant 8°C conditions for approximately 24 hr before sampling at 18:30. n = 2–8; average = 4.4.

(E) *FLC* expression averaged over all the time points of sampling day after 4 weeks cold. Kruskal-Wallis with Dunn's post hoc test between midday spike, night spike and spike memory (conditions with similar *VIN3* expression for the 4 weeks of the treatment to test for VIN3-independent effect only) gives $p<0.05$ significant difference (* in plot) between night spike and midday spike and between night spike and spike memory (no significant difference between midday spike and spike memory). Boxplots show median and 25th and 75th percentiles of the samples. Ends of whiskers show maximum and minimum values. n = 12–38; average > 30. In all cases, circle and bars show mean and standard error, respectively. RNA levels normalized to *UBC*, *PP2A*.

See also Figures S3 and S4.

properties assigned to them in the model presented in Figure S2A, other than the timescales that we knew they must satisfy from experimental data. Therefore, we found that an *LCD* model with temperature input at two timescales cannot reproduce the effect of the temperature spikes. To further demonstrate this point, we used the specific model of Figure S2A as an example and showed where it fails (Figures S3A–S3C).

This deficiency suggests the need for a further thermosensitive process: a short-term memory (*S*) of the temperature experienced by the plant. *S* reduces *VIN3* levels if warm temperatures have been experienced since the previous afternoon, consistent with the spike memory experiment and with the fact that a spike instead given the previous evening is still remembered the next day (Figures S4A and S4B). A more complicated alternative thermosensing structure might also be able to explain these data, for example, if *C*, as well as directly affecting *VIN3* transcription, also feeds into *D* (thus indirectly introducing temperature sensing at a third timescale, through *D*). However, here we define a more general case by introducing *S*, as described above.

S must act on *VIN3* transcription, since similar effects are seen for both spliced and unspliced *VIN3* (Figures 2B and 2C). Moreover, since unspliced *VIN3* levels respond immediately during and after the spike (Figure 2C, 12:30 data point in midday spike versus constant 12°C), this result still requires the presence of an immediate response (*C*) in addition to the short-term memory response of *S*. These two temperature-sensitive processes together combine to give the "absence of warmth response" that plants exhibit in vernalization thermosensing.

Our experiments also allowed us to derive further understanding about *L* and *C*. After a fixed period of constant temperature, levels of *VIN3* are anticorrelated with temperature (the graded

response mentioned in the previous section; Figures 2A–2D, "before"; Duncan et al., 2015; Wollenberg and Amasino, 2012). Conceptually, this effect could arise from either *L* building up more slowly at higher temperatures with a similar *C* or from *C* differentially affecting the transcription rate of *VIN3* at different temperatures but with the underlying *L* dynamics being similar (provided the temperature is sufficiently low). To distinguish between these possibilities, we studied plants treated with different cold temperature regimes but then brought together for a final day at a common temperature. We found that *VIN3* levels were different in the initial cold treatment (Figure 2D, "before"), as expected, but became similar on the final day (Figure 2D, "after"). This result clearly favors similar *L* dynamics but with fast-acting *C* responsible for higher *VIN3* transcription rates at lower temperatures.

Our results reveal distributed thermosensory inputs into *VIN3* expression, involving slow (*L*), intermediate (*S*), and fast (*C*) dynamics, as well as inputs from the circadian clock (*D*). The overall effect of the *LSCD* regulation of *VIN3* is a long-term memory of the length of cold, through *L*, which controls the amplitude of the diurnal *VIN3* peak (*D*) and which is further adjusted by daily temperature values, either immediate (*C*) or since the previous afternoon (*S*).

The *LSCD* Model for *VIN3* Thermosensing Can Explain *VIN3* Expression in the Lab and in the Field

We next added the short-term memory of warm spikes (*S*) process to our mathematical model for *VIN3* dynamics. The functional forms we chose to represent *L*, *S*, *C*, and *D* in our *LSCD* model are defined in Figures 3A, 3B, and S5 and STAR Methods. These functional forms and other parameters were fitted based on existing data from the literature (Hepworth et al., 2018; Figures 3C, 3D, 3E and S6A), as well as the data from Figures 2 and S7 (STAR Methods). This overall dataset includes both controlled and field experiments.

We chose forms for the temperature sensitivity that fitted our data and were simple to implement, but these are not unique, and indeed other forms could have been chosen, provided they had a similar shape in the ranges we investigated. More constraining were the timescales at which each pathway responded. Any plausible model must have temperature sensing at three timescales (long—month; short—day; current—hour), as well as diurnal variation, in order to explain our experimental observations. These three timescales are not tightly defined, with the exception of *S*, which appears to be tied to the 24-hr diurnal cycle. A 20% change in the timescale of *L* resulted in only a modest change in the agreement between the model and data (<5% change in relative error; see STAR Methods). Furthermore, *C* is here modeled as instantaneous, but the splicing rate of *VIN3* constrains the observed timescale of the current response, giving only an upper bound for the timescale of *C*. Therefore, a wide range of "Long" and "Current" timescales may be tolerated, but the two must be very well separated, being much longer and much shorter than a day, respectively.

The model could substantially reproduce the observed *VIN3* behavior in constant and complex temperature conditions, both in controlled and field conditions (Figures 3C, 3D, 3E, S6A, and S7). In particular, the model could recapitulate the *VIN3* behavior observed in the warm spike experiments (Figures S3D–S3F; relative likelihood of *LCD* compared to *LSCD* based on Akaike's information criterion: 5×10^{-7}; Figures S7E and S7F). In addition, the model also captured the substantial delay of *VIN3* upregulation in Norwich due to warm autumn days (Figure 3C), as well as a subtler delay in the first North Sweden planting (Figure 3D).

However, the field experiments also exhibited phenomena not seen in the controlled environment data that the model was unable to capture, including variable *VIN3* levels in the later stages of the 2014–2015 South Sweden data (Figure 3E). Field notes subsequently revealed that these plants had been buried under a mudslide during this time (Figure 3F), likely accounting for the divergence, since both hypoxia and light (indirectly, via circadian dynamics) regulate *VIN3* (Bond et al., 2009b; Hepworth et al., 2018). We were also unable to reproduce an apparent age effect between the two plantings in North Sweden 2014–2015 (Figures 3D and S6A), which we could not account for by temperature sensing alone since the plants were experiencing the same temperature conditions. Furthermore, the older plants (Figure 3D), which had experienced cold for longer, showed lower *VIN3*. Stress due to extreme cold conditions may have affected the younger plants more strongly than their older counterparts, leading to the observed effect.

The model predicted large fluctuations from day to day in the "model daily" *VIN3* levels in the spring (Figures 3C–3E). However, we do not have samples at high enough resolution to test if this was indeed the case in the field. Nevertheless, our predictions are consistent with the spring field samples we do have, as well as with results from our controlled experiments, such as for single days without a spike (spike memory) (Figure 2B), and also when a spike is introduced for the first time on the day of sampling (5°C with single spike) (Figure S7E and S7F).

FLC Downregulation Is Sensitive to Diurnal Timing, while *VIN3* Dynamics Are Not

We next turned to investigate the effect of temperature on *FLC* expression, mediated either through VIN3-dependent or -independent pathways. Above, we found that *VIN3* expression was reduced by a spike of high temperature regardless of when that spike was applied, provided the spike occurred since the previous afternoon. We therefore examined the response of *FLC* to such spikes. In a previous study, we found that *FLC* is downregulated more in fluctuating 14.2°C conditions than constant 14.2°C, despite fluctuating 14.2°C conditions having lower *VIN3* levels. This is due to the effect of the VIN3-independent pathway, which represses *FLC* at low temperatures, with lower temperatures being more repressive (Figure 2E; Hepworth et al., 2018). Consistently, we found that fluctuating 14.2°C conditions had a similar level of downregulation as both constant 12°C and midday spike conditions (Figure 2E). However, despite having the same mean temperature and similar *VIN3* expression profile as the midday spike (and also spike memory, which is treated identically to the midday spike for the 4 weeks prior to the day of sampling), the shift of the spike by 12 hr in the night spike impeded *FLC* repression (Figure 2E; Kruskal-Wallis with Dunn's post hoc test $p < 0.05$) Furthermore, in the *vin3-4* mutant, the night spike treatment also impeded repression (Figure S4D). These results suggest that the pathway controlling VIN3-independent transcriptional downregulation of *FLC* is gated in a diurnal, light-dependent, or circadian manner.

A

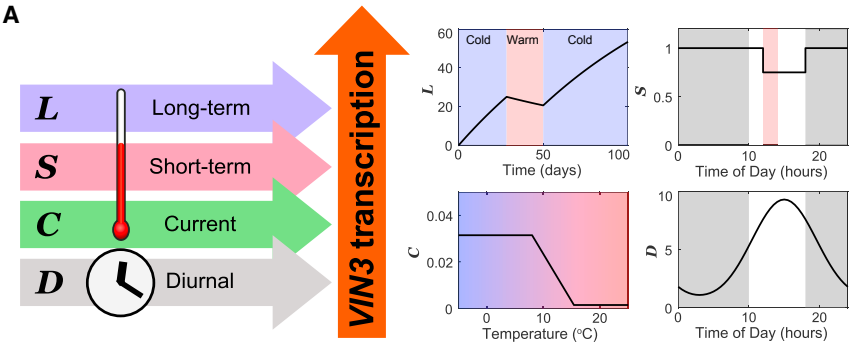

B

Unspliced *VIN3* concentration (v):

$$\frac{dv}{dt} = p_v(L,S,C,D) - s_v v$$

Spliced *VIN3* concentration (V):

$$\frac{dV}{dt} = s_v v - d_V V$$

where $p_v(L,S,C,D) = LSCD$ is the productive transcription, s_v is the splicing rate and d_V is the degradation rate of spliced *VIN3*.

Long-term (L)

$$\frac{dL}{dt} = \begin{cases} 1 - d_L L, & T < 17^oC \\ -d_L L, & T \geq 17^oC \end{cases}$$

Short-term (S)

$$S(T_m) = \begin{cases} 1, & T_m < 15^oC \\ S_1, & T_m \geq 15^oC \end{cases}$$

where T_m is the maximum temperature since the last resetting (4pm).

Current (C)

$$C(T) = \begin{cases} p_{C1}, & T \leq 8^oC \\ c(T), & 8^oC < T < 15.4^oC \\ p_{C1} - p_{C2}, & T \geq 15.4^oC \end{cases},$$

where

$$c(T) = p_{C1} - \frac{T-8}{15.4-8} p_{C2}$$

Diurnal (D)

$$D(t) = \left[p_D + \sin\left(2\pi \left(t - \frac{t_m - 1}{24} \right) \right) \right]^2$$

where t_m is the time at dawn.

C

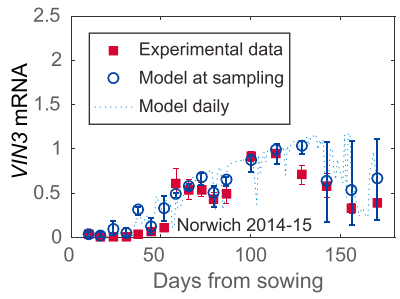

D

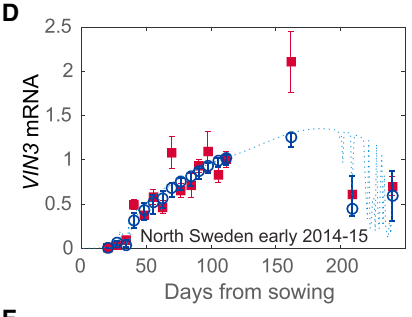

E

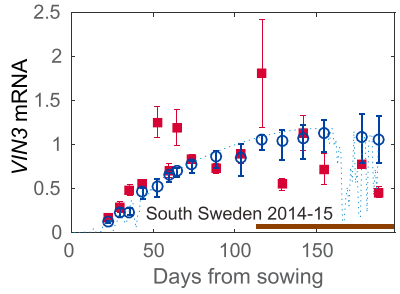

F

Figure 3. Description and Fitting of *LSCD* Model for *VIN3* Dynamics

(A) Diagram of the *LSCD* model showing the primary signals registered by each component, their temperature dependence, and how they affect *VIN3* transcription. Element *L* increases slowly in the cold (<17°C) and decreases slowly in the warm. Element *S* remembers the presence of a high temperature spike until the evening and, during that time, remains decreased. Element *C* is high at low temperatures and low at high temperatures, changing linearly with temperature between 8°C and 15.4°C. Element *D* cycles each day, peaking in the afternoon.

(B) Mathematical description of *LSCD* model showing the temperature and time dependency of each component.

(C) Comparison of *LSCD* model and fitted experimental *VIN3* mRNA data for Norwich in 2014–2015. Data from Hepworth et al. (2018), bars show mean and standard error, respectively. Model at sampling shows the mean of the predicted values of *VIN3* mRNA in the sampling time window, which is defined as the period from 2 hr before the recorded sampling time to 2 hr after due to the long duration of sampling. The error bars show the maximum and minimum values of *VIN3* mRNA during that time window. Model daily shows the predicted value for *VIN3* mRNA at the same time every day (chosen as the time of the final sampling) to demonstrate the changes in amplitude of the *VIN3* daily peak.

(D) Comparison of model and experimental data from North Sweden (early planting) in 2014–2015, as described for Norwich in (C).

(E) Comparison of model and experimental data from South Sweden in 2014–2015, as described for Norwich in (C). The late time points of the South Swedish data (brown bar) could not be fitted by our model, likely due to a mudslide (time given by start of brown bar) that damaged the plants and affected their *VIN3* expression.

(F) Mudslide at the South Swedish site covered the plants and caused sample losses.

See also Figures S1–S3 and S5–S7.

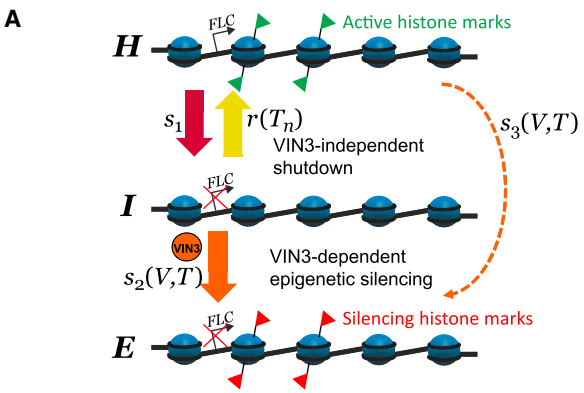

B

Fraction of *FLC* copies in high transcription (H), inactive (I) and epigenetically silent (E) states, so that $H + I + E = 1$, and concentration of spliced *FLC* [*FLC*]:

$$\frac{dH}{dt} = -s_1 H + r(T_n)I - s_3(V,T)H \qquad \frac{dE}{dt} = s_2(V,T)I + s_3(V,T)H$$

$$\frac{dI}{dt} = s_1 H - r(T_n)I - s_2(V,T)I \qquad \frac{d[FLC]}{dt} = p_f\left(\frac{H}{H_0} - [FLC]\right)$$

$$s_3(V,T) = 0.1 s_2(V,T), \qquad s_2(V,T) = \begin{cases} p_s V\,(T+1)(18-T), & -1^oC < T < 18^oC \\ 0, & T \le -1^oC \text{ or } T \ge 18^oC \end{cases}$$

where T is temperature, V is the *VIN3* concentration, and

$$r(T_n) = \begin{cases} 0, & T_n \le 11.5^oC \\ p_r \frac{T_n - 11.5}{15 - 11.5}, & 11.5^oC < T_n < 15^oC \\ p_r, & T_n \ge 15^oC \end{cases}$$ where T_n is the night temperature.

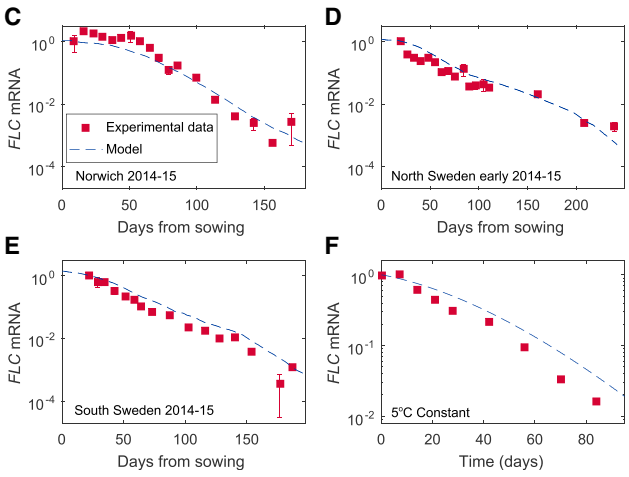

Figure 4. Description and Fitting of Model for *FLC* Dynamics

(A) Diagram of the *FLC* model showing switching between digital states in the *FLC* silencing pathway during vernalization.

(B) Mathematical description of *FLC* model showing the temperature dependency of the switches.

(C) Comparison of *FLC* model and fitted experimental *FLC* mRNA data for Norwich, in 2014–2015 (data from Hepworth et al. [2018]).

(D) Comparison of *FLC* model and experimental data for North Sweden (early planting) in 2014–15 (data from Hepworth et al. [2018]).

(E) Comparison of *FLC* model and experimental data for South Sweden in 2014–15 (data from Hepworth et al. [2018]).

(F) Comparison of *FLC* model and fitted experimental *FLC* mRNA data for Constant 5°C (combined data from Figure S9B).

In all cases, squares and bars show mean and standard error, respectively. See also Figures S5, S6, S8, and S9.

To distinguish between these possibilities, we designed further temperature spike regimes with spikes in the morning, just before subjective day, or in the evening, just after the onset of subjective night (both in the dark). While these spikes again affected *VIN3* similarly, they had different effects on *FLC* (Figure S4): the morning spike and midday spike conditions were as effective for *FLC* downregulation as constant 12°C, despite the former treatments having higher average temperatures (12.75°C). However, the evening spike conditions were less repressive, and the night spike conditions repressed significantly less than the morning and midday spikes (Figures S4C–S4F; Kruskal-Wallis with Dunn's post-hoc test, $p < 0.05$). The similar effects on *FLC* expression of the morning (in the dark) and midday (in the light) spikes suggest that light is not the gating factor. Overall, these results support a role for diurnal or circadian dynamics in the VIN3-independent pathway, with *FLC* repression being particularly sensitive to night-time temperatures.

Mathematical Model for *FLC* Must Include Multiple Thermoresponsive Steps

We next constructed a more extensive vernalization model, representing the dynamics of *FLC*, incorporating both VIN3-dependent (derived from the *VIN3* model above) and VIN3-independent pathways. A conceptual outline of the *FLC* module is shown in Figure 4A, based on previous experimental results (Angel et al., 2011, 2015). Unlike the *LSCD* model, which represents the action of inferred thermosensory processes on *VIN3* transcription, the *FLC* model consists of a series of digital states of the *FLC* gene that define its transcriptional state (Angel et al., 2011, 2015; Berry et al., 2015), together with various transitions between the states. Only the first state (*H*, high transcription) is transcriptionally active. Gene copies in the *H* state can switch to a transcriptionally inactive state *I*, inactive) through a VIN3-independent pathway (Csorba et al., 2014; Helliwell et al., 2011; Hepworth et al., 2018; Swiezewski et al., 2009). The mechanistic basis of the VIN3-independent pathway is still to be fully resolved but is likely to involve the functionality of non-coding *COOLAIR* antisense transcription or of the resulting transcripts (Csorba et al., 2014; Rosa et al., 2016; Swiezewski et al., 2009). Gene copies in the *I* state can then switch irreversibly to an epigenetically stable OFF state (*E*, epigenetically silenced) with a rate that depends on the cold-induced VIN3 level (Yang et al., 2017). We also included an additional VIN3-dependent transition directly from *H* to *E* to allow epigenetic silencing of *FLC* in the absence of VIN3-independent *FLC* downregulation, but at a much slower rate than for the *I* to *E* transition (Buzas et al., 2011). Ordinary differential equations were used to capture the dynamics of the relative proportions of gene copies in each state over the whole plant (Figure 4B). Each gene copy switches states independently of other copies within the same cell or in surrounding cells (Berry et al., 2015).

The *FLC* model was parameterized using a wide variety of data from the literature (Duncan et al., 2015; Hepworth et al., 2018; Yang et al., 2017; Figures 4C, 4D, 4E, 4F, S6B, and S8), including 2014–2015 field data and the data presented in this paper (Figures 2, S4, and S9). The VIN3-independent part of the model was parameterized based on data from the *vin3-4*, *vrn5-8*, and *vrn2-1* mutants (Figures S4 and S8; Hepworth et al., 2018; Yang et al., 2017), where the PRC2-based switches to *E* are blocked. The VIN3-independent transition from *H* to *I* is

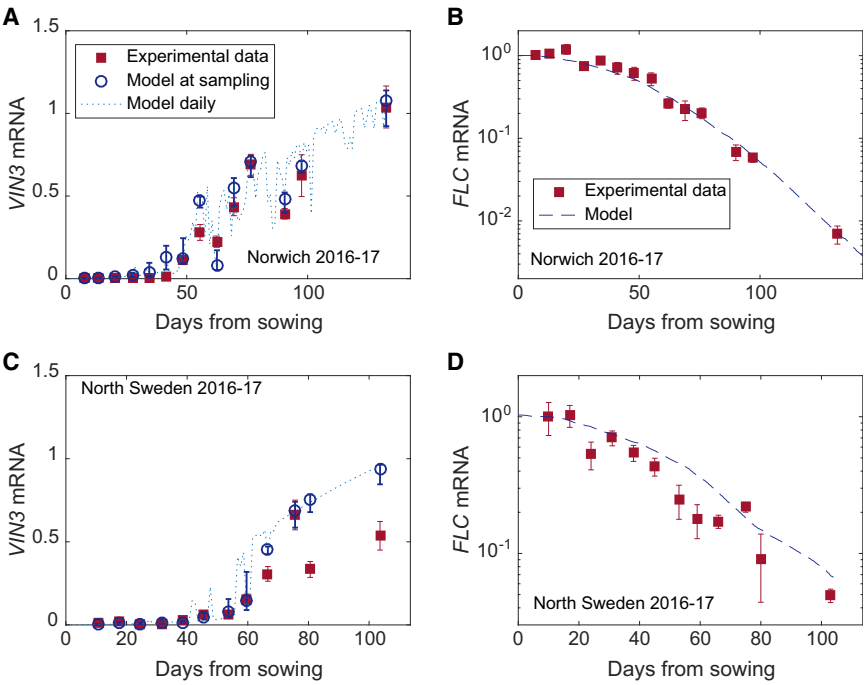

Figure 5. Validation of *VIN3/FLC* Model

(A and B) Validation of *VIN3/FLC* model by prediction of (A) *VIN3* and (B) *FLC* behavior under new field conditions in Norwich 2016–2017. n = 4–6; average > 5.4.

(C and D) As for (A) and (B) for new field conditions in North Sweden 2016–2017. n = 3–6; average > 4.6. For data, squares and bars show mean and standard error, respectively, while for the model, circles show the mean of the predicted values of *VIN3* mRNA in the sampling time window and bars show the maximum and minimum values during that time window.

See also Figures S6 and S10.

reversible, since in the absence of epigenetic silencing, *FLC* levels reactivate in the warm (Gendall et al., 2001; Helliwell et al., 2011; Yang et al., 2017). Additionally, as shown above in Figures 2 and S4, *VIN3* levels are the same in the case of the midday and night spike treatments, but *FLC* levels are lower if the spike occurs during the day. The temperature-sensitive VIN3-independent dynamics of *FLC* (shown in the STAR Methods to be the *I* to *H* transition, *r*) are therefore taken to be controlled by night-time temperatures, defined as the 6 hr either side of subjective midnight. The rate of *r* is positively correlated with temperature in the range of "cool" temperatures (Figure 4B and STAR Methods), as can be inferred from the faster rate of shutdown at colder temperatures in Figure S8.

In addition to the temperature dependence of *VIN3* dynamics, the *I* to *E* and *H* to *E* transitions are also directly temperature dependent. This feature is necessary to explain the absence of silencing in the warm in lines overexpressing *VIN3* (Kim and Sung, 2017; Lee et al., 2015), suggesting cold is necessary for the nucleation of epigenetic silencing. We also observed a difference in the rate of *FLC* downregulation at the different field sites, with the Swedish sites having slower downregulation despite higher levels of *VIN3* compared to Norwich (Hepworth et al., 2018). Consistently, vernalization has previously been found to be hindered by temperatures around 0°C or less (Duncan et al., 2015; Napp-Zinn, 1957; Wilczek et al., 2009). The model therefore incorporated direct temperature dependency in the *I* to *E* and *H* to *E* transitions, with an optimal temperature for epigenetic silencing and no silencing either above 18°C or below −1°C.

The overall mathematical model (Figure 4B; full description in STAR Methods) was successfully fitted to experimental *FLC* data for mutants (Figure S8) and wild-type plants (Col*FRI*^{SF2}) from the first field experiment (Figures 4C, 4D, 4E and S6B), as well as laboratory experiments (Figures 4F and S9). As in the *VIN3* model, temperature sensitivities enter in multiple places in the *FLC* model, supporting a hypothesis of distributed thermosensing, with routes to silenced *FLC* requiring temperature responsiveness at almost every step.

VIN3/FLC Model Can Predict Responses in the Field

To fully test our parameterized model, we challenged it with a second set of field data from winter 2016–2017. Experiments were repeated in North and South Sweden, as well as Norwich, UK but brought forward by 2 weeks to ensure that warmer field temperatures would fully test our predictions on temperature sensitivity. The effectiveness of the model was demonstrated by our ability to predict the behavior of *VIN3* and *FLC* in Norwich (Figures 5A and 5B), North Sweden (Figures 5C and 5D), and South Sweden (Figures S6C and S6D), without reparameterization.

Nevertheless, there were still aspects of these new datasets that could not be accounted for, in particular for *VIN3* (Figure 5C, late time points). Every day, *VIN3* levels start very low and peak in the afternoon. Therefore, the sampling time relative to this diurnal pattern is critical to correctly estimate the amplitude of the oscillations. In North Sweden 2016–2017, we found that the diurnal pattern of *VIN3* was shifted by several hours from that observed in controlled conditions or in Norwich 2016–2017 (Figures S10B, S10E, and S10H). This change meant that the peak of *VIN3* expression was much later than our sampling time, and therefore we were greatly underestimating its amplitude. This effect could, in part, explain the difference between our data and the model prediction after ~60 days in North Sweden (Figure 5C). The amplitude of the circadian clock gene *EARLY FLOWERING3* (*ELF3*) and both the amplitudes and phases of *LATE ELONGATED HYPOCOTYL* (*LHY*) and especially *CIRCADIAN CLOCK ASSOCIATED1* (*CCA1*) show differences between experimental sites and over time (Figure S10), which could be related to the cold (Bieniawska et al., 2008; Box et al., 2015; Gould et al., 2006) and which may explain this shift. However, due to the uncertainties regarding the behavior of the circadian clock under these fluctuating field conditions, we did not attempt to explain this changed behavior with a more complex model for *D*. Overall, despite some discrepancies, we conclude that the model could predict *VIN3* behavior, even in extremely challenging heterogeneous field conditions.

The results of the temperature fluctuations in the field are visible in the *VIN3* profile (e.g., Figure 5A), where short-term temperature dynamics feed through to influence *VIN3* expression. However, the slow, digital switching dynamics of *FLC* loci lead to noise filtering and to a smooth overall *FLC* expression profile, where sustained fluctuations affect the overall long-term rate of downregulation, but without a significant response of *FLC* to any specific temperature fluctuation event. Initially, *VIN3* levels are low, and therefore the VIN3-independent pathway dominates the *FLC* dynamics. In a later phase, where *VIN3* levels increase significantly, the rate of shut-down of *FLC* also tends to increase. Both years in Norwich and in North Sweden 2016–2017, the temperature conditions are such that an increase from low to high *VIN3* levels happens abruptly, leading to a clear separation of the two phases (Figures 3C, 4C, and 5). In 2014–2015 in Sweden, levels of *VIN3* increase quickly right from the start of measurement (Figures 3D, 3E, 4D, 4E, S6A, and S6B). Small changes to the rate of *FLC* repression do subsequently occur in Sweden due to further increase of *VIN3* levels. However, at the same time, lower temperatures directly reduce the efficiency of the transition to an epigenetically silenced state. These two effects substantially cancel out, effectively leading to a single, approximately exponential, *FLC* mRNA decay profile in the field (Figures 4D, 4E, and S6B).

In summary, we found substantive agreement between the model and our experiments, with the model showing significant predictive skill despite the intricate, fluctuating nature of the field temperature signal. Naturally, we cannot exclude the existence of other mechanisms that could explain this behavior. Nevertheless, the fact that our model can reproduce data collected from a wide range of conditions (including from field and various controlled-temperature profiles, from this paper, and from the literature) demonstrates that the model can be a powerful predictive tool.

Both Warmer and More Variable Temperatures Affect Vernalization

Having established that the *VIN3*/*FLC* combined model can predict responses to field conditions, we next examined which features of the field temperature profile it is most sensitive to by altering the temperature input. We first compared the results from the full temperature profile for Norwich 2014–2015 with that under a simplified treatment (day-mean) where the temperature profile each day is replaced by the mean value of that day (Figures 6A, 6B, 6C, 6D, 6E, 6F and S11A) for Col*FRI*^{SF2} (the wild-type line, "Col*FRI*"). We find that, over an early period (Figure 6F), the absence of cold temperatures in the day-mean profile (Figure 6D) leads to slower simulated *FLC* downregulation, partly due to the VIN3-independent pathway being less activated. However, later in winter, the absence of daily warm spikes in the day-mean treatment (Figure 6A) causes simulated *VIN3* levels to be higher (Figure 6C), leading to lower simulated *FLC* levels (Figure 6E).

To more clearly distinguish these differing effects of the VIN3-dependent and -independent pathways, we also simulated the behavior of a *vin3* null mutant (Figures 6E and 6F). In this case, as expected, we observed a significant impediment in the later simulated downregulation of *FLC*, as this mutant was blocked in epigenetic silencing. Once again, the day-mean treatment gave slower simulated downregulation in early winter (Figure 6F), confirming that this was due to the VIN3-independent pathway. Furthermore, a decrease in the frequency of low temperatures in the late period (Figure 6D) led to simulated reactivation of *FLC* in the *vin3-4* mutant much earlier under the day-mean treatment (Figure 6E).

We then modified the temperatures measured in the field to test what type of future climate changes might have the most significant effects on *FLC* expression. We first changed the mean temperatures while keeping the absolute size of the temperature fluctuations the same by adding 3°C to the entire field temperature profile (with the exception of temperatures around 0°C, when the plants are mainly covered by snow; STAR Methods). Such a change is within the predicted range of temperature increases for the end of this century (IPCC, 2014). In Norwich, this intervention strongly impeded simulated upregulation of *VIN3* and downregulation of *FLC* expression, as expected (Figures 6G, 6H, 6I and S11B) since both the frequency and magnitude of high temperature spikes were increased (Figure 6G), while the frequency and magnitude of low temperature dips were reduced (Figure 6H). On the other hand, in North Sweden (Figure S11D), there was very little difference in the presence of cold (Figure 6J) or warm (Figure 6K) following this modification. As a result, simulated *VIN3* and *FLC* both behaved similarly in the modified and original temperature profiles (Figure 6L). Interestingly, in the late phase of vernalization in Sweden (after ~100 days), slightly faster simulated *FLC* shutdown could be observed in the case of added 3°C. This effect arose because temperatures close to 0°C and lower hinder vernalization (Duncan et al., 2015; Napp-Zinn, 1957; Wilczek et al., 2009). Therefore, the increased but still low temperatures of the modified profile for Sweden are closer to the optimal range for *FLC* downregulation.

In comparison, stretching the field temperature profile T above and below the daily mean temperature (T_m) for each day ($T \rightarrow 2 \times (T - T_m) + T_m$), i.e., keeping the mean temperatures unchanged while increasing the fluctuations, had a smaller but still visible effect (Figures 6G, 6H, 6I, 6J, 6K, 6L, S11C, and S11E). This effect was even smaller in the case of the *vin3-4* mutant, where *FLC* decreased only due to the VIN3-independent pathway, for which the presence of cold was the driving mechanism. The stretch treatment did not increase the proportion of cold in the profile by much and therefore had little effect on the VIN3-independent pathway (Figures 6H and 6K). However, in Norwich, simulated *VIN3* expression was lower in the stretch treatment, especially at later times due to the increase of the warm spikes, and this effect led to a slower simulated shutdown of *FLC* in the wild-type. The simulated epigenetic shutdown of *FLC* was even further impeded by the very low temperatures in the stretch treatment at those late times (Figure S11C).

For both modifications to the temperature profile, we see an effect on simulated *FLC* shutdown. A 10-fold decrease in *FLC* mRNA concentration compared to its starting level is predicted to be reached on the 87th day in Norwich for 2014–2015. In the ×2 treatment, this is reached with a 4-day delay, while in the +3 treatment a 22-day delay is predicted. For a 100-fold decrease in *FLC* level, which in Norwich 2014–2015 is predicted to be reached on the 126th day, the delays have increased to 14

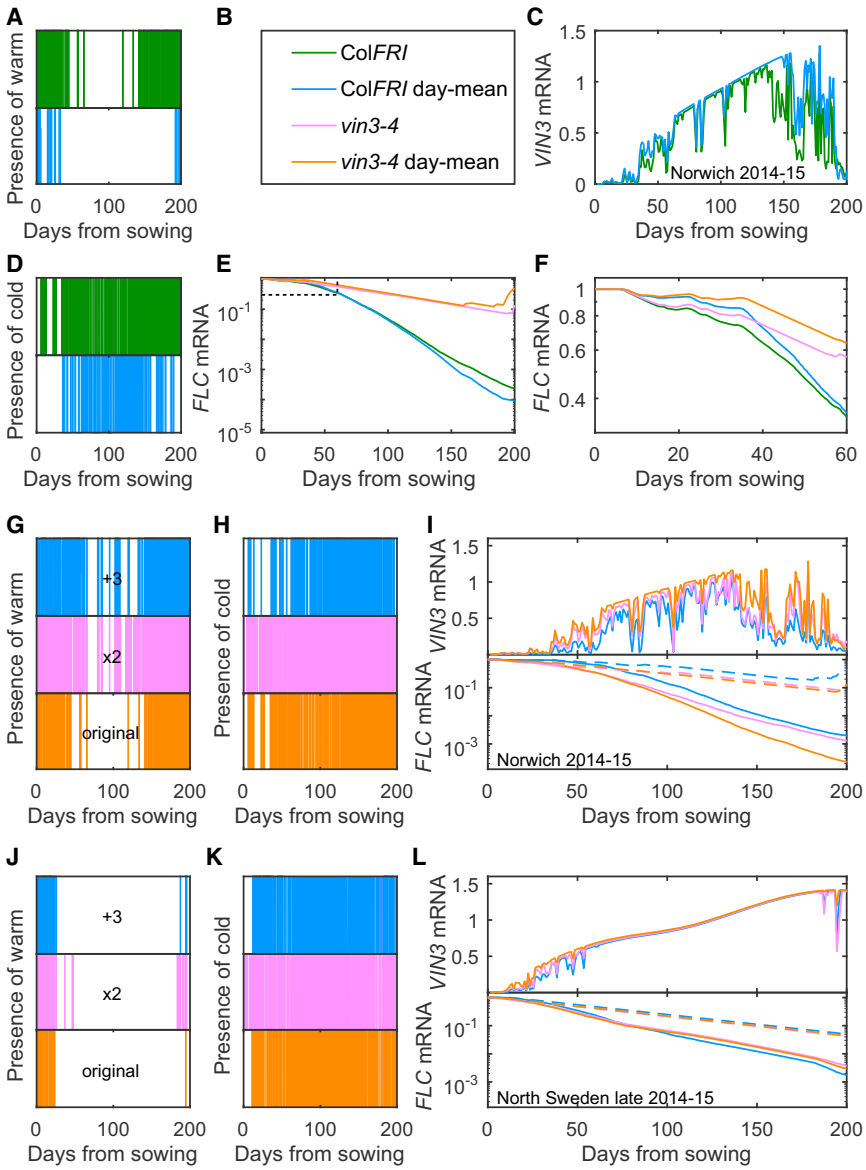

Figure 6. Assessment of Climate Sensitivity of *FLC* and *VIN3* Dynamics

(A–F) Norwich 2014–2015 prediction for Col*FRI*^{Sf2} (Col*FRI*, green) compared to the prediction where the temperature at each time point is replaced by the 24-hr average temperature of that day (Col*FRI* day-mean, blue). The same is shown also for the *vin3-4* mutant (pink and orange, respectively). (A) shows "presence of warm" features in the two temperature profiles, green for measured temperature, and blue for day-mean temperature. Presence of color stripe corresponds to a high temperature spike on that day (day maximum above 15°C). (B) Figure legend for (A)–(F). (C) *VIN3* mRNA prediction, for Col*FRI*. (D) shows "presence of cold" features in the two temperature profiles, green for measured temperature and blue for day-mean temperature. Presence of color stripe corresponds to a low temperature dip on that day (day minimum below 10°C). (E and F) *FLC* mRNA prediction, for ColFRI and *vin3-4* mutant. (F) shows the same predictions as (E) but only for the first 60 days, as indicated by dashed line square in (E).

(G) "Presence of warm" features in three temperature profiles, Norwich 2014–2015 (orange), the Norwich profile modified by adding 3°C ("+3," blue) or by stretching the temperatures around the daily mean ("x2," pink).

(H) "Presence of cold" features in the modified temperature profiles as described in (G).

(I) *FLC* and *VIN3* mRNA predictions based on Norwich 2014–2015 temperature (orange) compared to the modified profiles as in (G) and (H). Dashed lines are for *vin3-4* mutant.

(J) "Presence of warm" features in three temperature profiles, North Sweden 2014–2015 (orange), the North Sweden profile modified by adding 3°C ("+3," blue) or by stretching the temperatures around the daily mean ("x2," pink).

(K) "Presence of cold" features in the modified temperature profiles as described in (J).

(L) *FLC* and *VIN3* mRNA predictions based on North Sweden 2014–2015 temperature (orange) compared to the modified profiles as in (J) and (K). Dashed lines are for *vin3-4* mutant.

In all cases, temperatures are from Hepworth et al., (2018).

See also Figure S11.

and 27 days, respectively. These results suggest that two potential effects of climate change, general warming and increased temperature fluctuations, will both negatively affect the efficiency of vernalization.

DISCUSSION

In this work, we investigated the temperature sensitivity of the major regulators of vernalization, *VIN3* and *FLC*, and then exploited this information to construct a modular mathematical model of the vernalization process. We used an experiment-driven approach, logically extracting from our data the features and timescales that an underlying model must include. We chose functional forms in the model that could reproduce our data and represent the observed varied temperature sensing. Our *VIN3*/*FLC* model could then in most circumstances accurately predict *VIN3* and *FLC* response to temperature in the field, although we were not able to capture some aspects of age and diurnal response.

In developing the model, we identified a need for multiple, distributed thermosensory inputs into *VIN3* and *FLC* and progressed our understanding of which aspects of the temperature signal each step was sensitive to. In fact, we found that most steps (L, S, C, VIN3-independent (r), VIN3-dependent (s_2,s_3)) of the vernalization pathway had to be temperature sensitive. For the remaining steps, it was not necessary to include temperature sensitivity, but there was no evidence to suggest that such sensitivity could not exist. Multiple temperature sensitivities have also been found in the regulation of the gene *FT* (Kinmonth-Schultz et al., 2018). Such distributed thermosensing is in contrast to an alternative hypothesis where thermal response is proposed

to be governed by a small number of core thermosensors (Quint et al., 2016; Wigge, 2013). We find this latter hypothesis to be generally less likely due to the global temperature dependence of biochemistry. Furthermore, an isolated thermosensor would require the remainder of the network to be temperature compensated, a situation that would not be straightforward to achieve. For these reasons, we expect that temperature sensing will be fundamentally different from sensing other environmental signals such as light perception, where isolated, specialized sensors are certainly required.

In our analysis, we identified a new thermosensing element: short-term memory of warm spikes (*S*). Its behavior is consistent with a response to warm temperatures that resets its short-term memory every evening. Indeed, in Figure 2B, at the first time point after dusk, the levels of *VIN3* in treatments with a temperature spike were reset to the levels of treatments with constant background temperature, suggesting that the circadian clock is involved. *VIN3* is also regulated directly by the clock, through *D*, consistent with the known binding of the circadian regulator CCA1 to the *VIN3* promoter (Nagel et al., 2015).

From our analysis, we cannot exclude the possibility that there is cross-talk between the thermosensor pathways *L*, *S*, and *C* and indeed that some factors may be common between them. However, the key result is that they must be distinct in their response, as they sense temperature at different timescales. At present, there are no clear candidates for *L*, *S*, and *C* (Bond et al., 2009a, 2009b, 2011; Finnegan et al., 2011). Instead, focused genetic screens in specific temperature regimes will need to be undertaken to identify these components. However, we expect that the detailed dissection of their properties carried out here should greatly facilitate their molecular identification.

This work also confirms our earlier proposal (Hepworth et al., 2018) that the *L* element acts similarly to the "day-degree" element used in agricultural crop modeling, recording time within a temperature interval rather than the temperature itself (Aikawa et al., 2010; Chew et al., 2012; Wang et al., 2002, 2017; Weir et al., 1984). Elements *C* and *S* then add information on current and recent temperatures to the *VIN3* system, responding rapidly to current and recent conditions. This combination of long-term (*L*) and shorter-term (*C* and *S*) temperature monitoring provides a sophisticated mechanism to distinguish between autumn and winter, even in the presence of large seasonal temperature fluctuations. This ability is generated by multiplicative regulation of *VIN3* by the thermosensing elements; if any are low, then the *VIN3* levels are also low. Under normal conditions, in autumn, plants have not experienced cold for long enough to accumulate high levels of *L*. However, should *L* accumulate to high levels early due to inadvertent early germination, the fast response due to *S* and *C* will be sufficient to keep *VIN3* levels low until temperatures stop spiking to high levels daily. On the other hand, in the case of an unusually cold autumn, when *S* and *C* may be high, low levels of the *L* thermosensor will act as a break early on, delaying the response of *VIN3*.

The importance of deepening our understanding of how fluctuations affect temperature responses has been widely recognized (Chew et al., 2012; Hepworth et al., 2018; Sidaway-Lee et al., 2010; Topham et al., 2017). The slow dynamics of *L* and the digital nature of the epigenetic pathway of *FLC* shutdown combine to give a highly effective integration over the noisy temperature signal. However, we also find that the warm sensitivity of *S* and *C* combine to make the VIN3-dependent pathway particularly sensitive to warm spikes in temperature during the autumn in the field. In the present climate, this effect is largely compensated for by the VIN3-independent pathway, which responds to the cold nights of autumn and represses *FLC* transiently. In modeling future climates, we find that higher temperatures due to global warming are likely to lead to a decrease in repression provided by both the VIN3-dependent and VIN3-independent pathways in climates such as Norwich (Figures 6G–6I). However, the same temperature change in Sweden is not predicted to have as strong an effect on vernalization in the synthetic accession we analyzed in this study (Figures 6J–6L). In fact, the model shows that an increase of temperature would lead to less extreme cold temperatures, bringing the temperature profile closer to the vernalization optimum and therefore paradoxically accelerating *FLC* shutdown.

To make more realistic predictions of vernalization under future climates, it will be informative to utilize climate model projections. However, we find that warm temperature spikes of even a short duration can have dramatic effects on vernalization. It will therefore be necessary to use very high temporal resolution temperature profiles for the predictions. Furthermore, it will be important to consider the local microenvironment of the vernalizing plant tissues. For *Arabidopsis*, it will be the temperature at the soil surface that is most relevant and often in direct sunlight. Temperatures in such a microenvironment may be significantly different from the temperatures observed even 1 m above the soil or in the shade, particularly with reference to the absence of short-term warm spikes. Integrating models of the type described in this paper with appropriate climate projections will therefore be a significant challenge for future studies.

STAR★METHODS

Detailed methods are provided in the online version of this paper and include the following:

- KEY RESOURCES TABLE
- CONTACT FOR REAGENT AND RESOURCE SHARING
- EXPERIMENTAL MODEL AND SUBJECT DETAILS
  - Replicate Numbers
  - Field Experiments
  - Laboratory Experiments
- METHOD DETAILS
  - RNA Preparation and QPCR
  - smFISH
  - Probe Design
  - Sample Preparation
  - Probe Hybridization
  - Image Acquisition
  - smFISH RNA Count Quantification
  - Mathematical Models
- QUANTIFICATION AND STATISTICAL ANALYSIS
  - Experimental Data Comparison
  - Mathematical Model Optimisation
  - Model Sensitivity to the Long-Term Timescale
  - *VIN3* Model Comparison Using AIC
- DATA AND SOFTWARE AVAILABILITY

SUPPLEMENTAL INFORMATION

Supplemental Information includes eleven figures and six tables and can be found with this article online at https://doi.org/10.1016/j.cels.2018.10.011.

ACKNOWLEDGMENTS

Thanks to Dr. Hongchun Yang (Wuhan University) for providing us with his data to parameterize the model. Thanks to Alex Coates who did preliminary work on the *FLC* model. Great thanks to family Öhman and Nils Jönsson for the experimental field sites in Sweden. In Norwich, thanks to Dr. Judith Irwin, Huamei Wang, Catherine Taylor and JIC Horticultural Services, and the entire Dean group and friends for help with the field experiments. Thanks to Professor Enrico Coen, Dr. Cecilia Lövkvist, Dr. John Fozard, Dr. Giuseppe Facchetti (John Innes Centre), Dr. Akiko Satake (Kyushu University), and Prof. Hiroshi Kudoh (Kyoto University) for useful discussion and comments on the manuscript, and to Ingalill Thorsell of Drakamöllan Gårdshotell for hosting many key discussions. This work was funded by the European Research Council grant MEXTIM and supported by the BBSRC Institute Strategic Programmes GRO (BB/J004588/1) and GEN (BB/P013511/1). Finally, the authors would like to reiterate their thanks to all those acknowledged in Hepworth et al. (2018), whose work underpins this paper.

AUTHOR CONTRIBUTIONS

R.L.A.-K. contributed to methodology, investigation, and analysis for field experiments, and Figures 2, S1, S7, and S9; J.H. to methodology, investigation, and analysis for field experiments and Figure S4; R.L.A.-K. and M.H. to mathematical modeling; S.H. and T.S. to methodology and investigation for field experiments in North and South Sweden, respectively; A.H., J.Q., and S.D. to methodology and investigation for fitting experiments (Figure S9); S.D. and S.R. to methodology, investigation, and analysis for smFISH (Figure S1); C.D. and M.H. to the concept of research, supervision, and analysis. R.L.A.-K., J.H., C.D., and M.H. wrote the paper.

DECLARATION OF INTERESTS

The authors declare no competing interests.

Received: June 28, 2018
Revised: August 15, 2018
Accepted: October 25, 2018
Published: November 28, 2018

REFERENCES

Aikawa, S., Kobayashi, M.J., Satake, A., Shimizu, K.K., and Kudoh, H. (2010). Robust control of the seasonal expression of the Arabidopsis FLC gene in a fluctuating environment. Proc. Natl. Acad. Sci. USA *107*, 11632–11637.

Andrés, F., and Coupland, G. (2012). The genetic basis of flowering responses to seasonal cues. Nat. Rev. Genet. *13*, 627–639.

Angel, A., Song, J., Dean, C., and Howard, M. (2011). A Polycomb-based switch underlying quantitative epigenetic memory. Nature *476*, 105–108.

Angel, A., Song, J., Yang, H., Questa, J.I., Dean, C., and Howard, M. (2015). Vernalizing cold is registered digitally at FLC. Proc. Natl. Acad. Sci. USA *112*, 4146–4151.

Berry, S., Hartley, M., Olsson, T.S.G., Dean, C., and Howard, M. (2015). Local chromatin environment of a Polycomb target gene instructs its own epigenetic inheritance. Elife *4*, e07205.

Bieniawska, Z., Espinoza, C., Schlereth, A., Sulpice, R., Hincha, D.K., and Hannah, M.A. (2008). Disruption of the Arabidopsis circadian clock is responsible for extensive variation in the cold-responsive transcriptome. Plant Physiol. *147*, 263–279.

Bloomer, R.H., and Dean, C. (2017). Fine-tuning timing: natural variation informs the mechanistic basis of the switch to flowering in Arabidopsis thaliana. J. Exp. Bot. *68*, 5439–5452.

Bond, D.M., Dennis, E.S., Pogson, B.J., and Finnegan, E.J. (2009a). Histone acetylation, VERNALIZATION INSENSITIVE 3, FLOWERING LOCUS C, and the vernalization response. Mol. Plant *2*, 724–737.

Bond, D.M., Wilson, I.W., Dennis, E.S., Pogson, B.J., and Jean Finnegan, E. (2009b). VERNALIZATION INSENSITIVE 3 (VIN3) is required for the response of Arabidopsis thaliana seedlings exposed to low oxygen conditions. Plant J. *59*, 576–587.

Bond, D.M., Dennis, E.S., and Finnegan, E.J. (2011). The low temperature response pathways for cold acclimation and vernalization are independent. Plant Cell Environ. *34*, 1737–1748.

Box, M.S., Huang, B.E., Domijan, M., Jaeger, K.E., Khattak, A.K., Yoo, S.J., Sedivy, E.L., Jones, D.M., Hearn, T.J., Webb, A.A.R., et al. (2015). ELF3 controls thermoresponsive growth in Arabidopsis. Curr. Biol. *25*, 194–199.

Buzas, D.M., Robertson, M., Finnegan, E.J., and Helliwell, C.A. (2011). Transcription-dependence of histone H3 lysine 27 trimethylation at the Arabidopsis polycomb target gene FLC. Plant J. Cell. Mol. Biol. *65*, 872–881.

Chew, Y.H., Wilczek, A.M., Williams, M., Welch, S.M., Schmitt, J., and Halliday, K.J. (2012). An augmented Arabidopsis phenology model reveals seasonal temperature control of flowering time. New Phytol. *194*, 654–665.

Csorba, T., Questa, J.I., Sun, Q., and Dean, C. (2014). Antisense COOLAIR mediates the coordinated switching of chromatin states at FLC during vernalization. Proc. Natl. Acad. Sci. USA *111*, 16160–16165.

De Lucia, F., Crevillen, P., Jones, A.M.E., Greb, T., and Dean, C. (2008). A PHD-polycomb repressive complex 2 triggers the epigenetic silencing of FLC during vernalization. Proc. Natl. Acad. Sci. USA *105*, 16831–16836.

Duncan, S., and Rosa, S. (2018). Gaining insight into plant gene transcription using smFISH. Transcription *9*, 166–170.

Duncan, S., Holm, S., Questa, J., Irwin, J., Grant, A., and Dean, C. (2015). Seasonal shift in timing of vernalization as an adaptation to extreme winter. Elife *4*, e06620.

Duncan, S., Olsson, T.S.G., Hartley, M., Dean, C., and Rosa, S. (2016). A method for detecting single mRNA molecules in Arabidopsis thaliana. Plant Methods *12*, 13.

Finnegan, E.J., Bond, D.M., Buzas, D.M., Goodrich, J., Helliwell, C.A., Tamada, Y., Yun, J.-Y., Amasino, R.M., and Dennis, E.S. (2011). Polycomb proteins regulate the quantitative induction of VERNALIZATION INSENSITIVE 3 in response to low temperatures. Plant J. Cell. Mol. Biol. *65*, 382–391.

Gendall, A.R., Levy, Y.Y., Wilson, A., and Dean, C. (2001). The VERNALIZATION 2 gene mediates the epigenetic regulation of vernalization in Arabidopsis. Cell *107*, 525–535.

Gould, P.D., Locke, J.C.W., Larue, C., Southern, M.M., Davis, S.J., Hanano, S., Moyle, R., Milich, R., Putterill, J., Millar, A.J., et al. (2006). The molecular basis of temperature compensation in the Arabidopsis circadian clock. Plant Cell *18*, 1177–1187.

Greb, T., Mylne, J.S., Crevillen, P., Geraldo, N., An, H., Gendall, A.R., and Dean, C. (2007). The PHD finger protein VRN5 functions in the epigenetic silencing of Arabidopsis FLC. Curr. Biol. *17*, 73–78.

Helliwell, C.A., Robertson, M., Finnegan, E.J., Buzas, D.M., and Dennis, E.S. (2011). Vernalization-repression of Arabidopsis FLC requires promoter sequences but not antisense transcripts. PLoS One *6*, e21513.

Hepworth, J., Antoniou-Kourounioti, R.L., Bloomer, R.H., Selga, C., Berggren, K., Cox, D., Collier Harris, B.R., Irwin, J.A., Holm, S., Säll, T., et al. (2018). Absence of warmth permits epigenetic memory of winter in Arabidopsis. Nat. Commun. *9*, 639.

IPCC, and C.W.T. (2014). IPCC Climate Change 2014: Synthesis Report. In Contribution of Working Groups I, II and III to the Fifth Assessment Report of the Intergovernmental Panel on Climate Change, R.K. Pachauri and L.A. Meyer, eds. (IPCC).

Irwin, J.A., Soumpourou, E., Lister, C., Ligthart, J.D., Kennedy, S., and Dean, C. (2016). Nucleotide polymorphism affecting FLC expression underpins heading date variation in horticultural brassicas. Plant J. *87*, 597–605.

Jones, E., Oliphant, T., Peterson, P., et al. (2001). SciPy: Open Source Scientific Tools for Python. http://www.scipy.org/.

Kemi, U., Niittyvuopio, A., Toivainen, T., Pasanen, A., Quilot-Turion, B., Holm, K., Lagercrantz, U., Savolainen, O., and Kuittinen, H. (2013). Role of vernalization and of duplicated FLOWERING LOCUS C in the perennial Arabidopsis lyrata. New Phytol. *197*, 323–335.

Kiefer, C., Severing, E., Karl, R., Bergonzi, S., Koch, M., Tresch, A., and Coupland, G. (2017). Divergence of annual and perennial species in the Brassicaceae and the contribution of cis-acting variation at FLC orthologues. Mol. Ecol. *26*, 3437–3457.

Kim, D.H., and Sung, S. (2017). The binding specificity of the PHD-finger domain of VIN3 moderates vernalization response. Plant Physiol. *173*, 1258–1268.

Kim, D.H., Zografos, B.R., and Sung, S. (2010). Vernalization-mediated VIN3 induction overcomes the LIKE-HETEROCHROMATIN PROTEIN1/POLYCOMB REPRESSION COMPLEX2-mediated epigenetic repression. Plant Physiol. *154*, 949–957.

Kinmonth-Schultz, H.A., MacEwen, M.J., Seaton, D.D., Millar, A.J., Imaizumi, T., and Kim, S.-H. (2018). Mechanistic model of temperature influence on flowering through whole-plant accumulation of FT. BioRxiv. https://doi.org/10.1101/267104.

Kudoh, H. (2016). Molecular phenology in plants: in natura systems biology for the comprehensive understanding of seasonal responses under natural environments. New Phytol. *210*, 399–412.

Lee, I., and Amasino, R.M. (1995). Effect of vernalization, photoperiod, and light quality on the flowering phenotype of Arabidopsis Plants containing the FRIGIDA gene. Plant Physiol. *108*, 157–162.

Lee, J., Yun, J.Y., Zhao, W., Shen, W.H., and Amasino, R.M. (2015). A methyltransferase required for proper timing of the vernalization response in Arabidopsis. Proc. Natl. Acad. Sci. USA *112*, 2269–2274.

Linkert, M., Rueden, C.T., Allan, C., Burel, J.M., Moore, W., Patterson, A., Loranger, B., Moore, J., Neves, C., MacDonald, D., et al. (2010). Metadata matters: access to image data in the real world. J. Cell Biol. *189*, 777–782.

Locke, J.C.W., Kozma-Bognár, L., Gould, P.D., Fehér, B., Kevei, E., Nagy, F., Turner, M.S., Hall, A., and Millar, A.J. (2006). Experimental validation of a predicted feedback loop in the multi-oscillator clock of Arabidopsis thaliana. Mol. Syst. Biol. *2*, 59.

MacGregor, D.R., Gould, P., Foreman, J., Griffiths, J., Bird, S., Page, R., Stewart, K., Steel, G., Young, J., Paszkiewicz, K., et al. (2013). *HIGH EXPRESSION OF OSMOTICALLY RESPONSIVE GENES1* Is Required for Circadian Periodicity through the Promotion of Nucleo-Cytoplasmic mRNA Export in Arabidopsis. Plant Cell *25*, 4391–4404.

Michaels, S.D., and Amasino, R.M. (1999). FLOWERING LOCUS C encodes a novel MADS domain protein that acts as a repressor of flowering. Plant Cell *11*, 949–956.

Nagel, D.H., Doherty, C.J., Pruneda-Paz, J.L., Schmitz, R.J., Ecker, J.R., and Kay, S.A. (2015). Genome-wide identification of CCA1 targets uncovers an expanded clock network in Arabidopsis. Proc. Natl. Acad. Sci. USA *112*, E4802–E4810.

Napp-Zinn, K. (1957). Untersuchungen über das Vernalisationsverhalten einer winterannuellen Rasse von Arabidopsis thaliana. Planta *50*, 177–210.

Qüesta, J.I., Song, J., Geraldo, N., An, H., and Dean, C. (2016). Arabidopsis transcriptional repressor VAL1 triggers Polycomb silencing at FLC during vernalization. Science *353*, 485–488.

Quint, M., Delker, C., Franklin, K.A., Wigge, P.A., Halliday, K.J., and van Zanten, M. (2016). Molecular and genetic control of plant thermomorphogenesis. Nat. Plants *2*, 15190.

Rosa, S., Duncan, S., and Dean, C. (2016). Mutually exclusive sense–antisense transcription at *FLC* facilitates environmentally induced gene repression. Nat. Commun. *7*, 13031.

Ruijter, J.M., Ramakers, C., Hoogaars, W.M., Karlen, Y., Bakker, O., van den Hoff, M.J., and Moorman, A.F. (2009). Amplification efficiency: linking baseline and bias in the analysis of quantitative PCR data. Nucleic Acids Res. *37*, e45.

Sanchez, S.E., and Kay, S.A. (2016). The plant circadian clock: From a simple timekeeper to a complex developmental manager. Cold Spring Harb. Perspect. Biol. *8*, a027748.

Satake, A., Kawagoe, T., Saburi, Y., Chiba, Y., Sakurai, G., and Kudoh, H. (2013). Forecasting flowering phenology under climate warming by modelling the regulatory dynamics of flowering-time genes. Nat. Commun. *4*, 2303.

Schneider, C.A., Rasband, W.S., and Eliceiri, K.W. (2012). NIH Image to ImageJ: 25 years of image analysis. Nat. Methods *9*, 671–675.

Shampine, L.F., and Reichelt, M.W. (1997). The MATLAB ODE suite. SIAM J. Sci. Comput. *18*, 1–22.

Sheldon, C.C., Burn, J.E., Perez, P.P., Metzger, J., Edwards, J.A., Peacock, W.J., and Dennis, E.S. (1999). The FLF MADS box gene: a repressor of flowering in Arabidopsis regulated by vernalization and methylation. Plant Cell *11*, 445–458.

Shrestha, R., Gómez-Ariza, J., Brambilla, V., and Fornara, F. (2014). Molecular control of seasonal flowering in rice, Arabidopsis and temperate cereals. Ann. Bot. *114*, 1445–1458.

Sidaway-Lee, K., Josse, E.M., Brown, A., Gan, Y., Halliday, K.J., Graham, I.A., and Penfield, S. (2010). SPATULA links daytime temperature and plant growth rate. Curr. Biol. *20*, 1493–1497.

Sung, S., and Amasino, R.M. (2004). Vernalization in Arabidopsis thaliana is mediated by the PHD finger protein VIN3. Nature *427*, 159–164.

Swiezewski, S., Liu, F., Magusin, A., and Dean, C. (2009). Cold-induced silencing by long antisense transcripts of an Arabidopsis Polycomb target. Nature *462*, 799–802.

Topham, A.T., Taylor, R.E., Yan, D., Nambara, E., Johnston, I.G., and Bassel, G.W. (2017). Temperature variability is integrated by a spatially embedded decision-making center to break dormancy in Arabidopsis seeds. Proc. Natl. Acad. Sci. USA *114*, 6629–6634.

Wales, D.J., and Doye, J.P.K. (1997). Global optimization by basin-hopping and the lowest energy structures of Lennard-Jones clusters containing up to 110 atoms. J. Phys. Chem. A *101*, 5111–5116.

Wang, E., Robertson, M.J., Hammer, G.L., Carberry, P.S., Holzworth, D., Meinke, H., Chapman, S.C., Hargreaves, J.N.G., Huth, N.I., and McLean, G. (2002). Development of a generic crop model template in the cropping system model APSIM. Eur. J. Agron *18*, 121–140.

Wang, E., Martre, P., Zhao, Z., Ewert, F., Maiorano, A., Rötter, R.P., Kimball, B.A., Ottman, M.J., Wall, G.W., White, J.W., et al. (2017). The uncertainty of crop yield projections is reduced by improved temperature response functions. Nat. Plants *3*, 17102.

Wang, R., Farrona, S., Vincent, C., Joecker, A., Schoof, H., Turck, F., Alonso-Blanco, C., Coupland, G., and Albani, M.C. (2009). PEP1 regulates perennial flowering in Arabis alpina. Nature *459*, 423–427.

Weir, A.H., Bragg, P.L., Porter, J.R., and Rayner, J.H. (1984). A winter wheat crop simulation model without water or nutrient limitations. J. Agric. Sci. *102*, 371–382.

Wigge, P.A. (2013). Ambient temperature signalling in plants. Curr. Opin. Plant Biol. *16*, 661–666.

Wilczek, A.M., Roe, J.L., Knapp, M.C., Cooper, M.D., Lopez-Gallego, C., Martin, L.J., Muir, C.D., Sim, S., Walker, A., Anderson, J., et al. (2009). Effects of genetic perturbation on seasonal life history plasticity. Science *323*, 930–934.

Wollenberg, A.C., and Amasino, R.M. (2012). Natural variation in the temperature range permissive for vernalization in accessions of Arabidopsis thaliana. Plant Cell Environ. *35*, 2181–2191.

Yang, H., Berry, S., Olsson, T.S.G., Hartley, M., Howard, M., and Dean, C. (2017). Distinct phases of Polycomb silencing to hold epigenetic memory of cold in Arabidopsis. Science *357*, 1142–1145.

STAR★METHODS

KEY RESOURCES TABLE

REAGENT or RESOURCE	SOURCE	IDENTIFIER
Chemicals, Peptides, and Recombinant Proteins		
Glucose oxidase	Sigma-Aldrich	Cat#G0543
Catalase	Sigma-Aldrich	Cat#C3155
Roche Universal Probe Library	Roche	N/A
SuperScript II Reverse Transcriptase	Life Technologies	Cat# 18064014
LightCycler® 480 SYBR Green I Master	Roche	Cat~ 04887352001
Critical Commercial Assays		
Stellaris FISH Custom Probes	LGC Biosearch Technologies (California, USA)	N/A
Deposited Data		
Raw microscopy data	This paper	figshare: https://doi.org/10.6084/m9.figshare.7346552
Experimental Models: Organisms/Strains		
Col *FRI*^{SF2}	Lee and Amasino (1995)	N/A
vin3-4 FRI^{SF2}	Bond et al. (2009b)	N/A
Oligonucleotides		
Primers for cDNA synthesis and qPCR (Table S1)	Hepworth et al. (2018); MacGregor et al. (2013)	N/A
Primers for qPCR (Table S2)	This paper	N/A
Stellaris Probes for smFISH (Table S3)	This paper	N/A
Software and Algorithms		
Stellaris Probe Designer version 2.0	LGC Biosearch Technologies (California, USA)	https://www.biosearchtech.com/support/tools/design-software/stellaris-probe-designer
FISHcounts	Duncan et al. (2016)	https://github.com/JIC-CSB/FISHcount
Bio-Formats	Linkert et al. (2010)	https://www.openmicroscopy.org/bio-formats/
ZEN	Zeiss	https://www.zeiss.com/microscopy/int/products/microscope-software/zen.html
SciPy	Jones et al. (2001); Wales and Doye (1997)	https://www.scipy.org
GraphPad Prism version 5.04 for Windows	GraphPad Software, San Diego, California, USA	www.graphpad.com
MATLAB R2016a	Shampine and Reichelt (1997)	N/A
LinRegPCR	Ruijter et al. (2009)	http://www.hartfaalcentrum.nl/index.php?main=files&fileName=LinRegPCR.zip&description=LinRegPCR:%20qPCR%20data%20analysis&sub=LinRegPCR
ImageJ	Schneider et al. (2012)	https://imagej.nih.gov/ij/
Other		
Zeiss Elyra PS1 inverted microscope	Zeiss	N/A
EM-CCD Andor iXon 897 camera	Andor	N/A

CONTACT FOR REAGENT AND RESOURCE SHARING

Further information and requests for resources and reagents should be directed to and will be fulfilled by the Lead Contact, Martin Howard (martin.howard@jic.ac.uk).

EXPERIMENTAL MODEL AND SUBJECT DETAILS

Replicate Numbers

Numbers of biological replicates that passed quality control (see Hepworth et al., 2018 for details) and were used for analysis are presented for all experiments in Table S6.

Field Experiments

The standard vernalization reference accession Col *FRI*^{SF2} and mutant *vin3-4 FRI* have been described previously (Bond et al., 2009a; Lee and Amasino, 1995). Field experiments were carried out as described in Hepworth et al. (2018) and Figure 1. For all field sites and sowing dates, for each timepoint, six replicate tray-cells were sown in a block-randomised design, with at least three plants sampled per replicate. Tissues sampled in Norwich were as shown in Figure 1; for Sweden, whole plants were sampled throughout. For Figure S8F, Norwich 2014-15 winter, plants were moved from the unlit, unheated 'field' glasshouse on 3rd December 2014 (65 days after sowing), or 7th January 2015 (100 days after sowing), to a greenhouse set to 22°C/18°C, 16 light/8 hour dark, and continued to be sampled with 3 replicates per timepoint.

For the 2016-2017 season, in Norwich plants were sown on 15th September 2016. In Sweden, plants were sown at Mid Sweden University (North Sweden) on 12th August 2016, and moved to the test site on 24th August 2016, and for South Sweden plants were sown on 6th September 2016 at Lund University and moved on 21st September 2016. For the 48hr sampling in the field, samples were prepared and randomised as for the long-term trials, with three replicates for Norwich and six for each Sweden site, and samples were taken once every four hours over the 48hr period of sampling.

Temperature was recorded at plant level at each site with TinyTag Plus 2 dataloggers (Gemini Data Loggers (UK) Ltd).

Laboratory Experiments

Plant Material for RNA Experiments

The aerial parts of whole plants were sampled at all times for controlled-condition experiments, with at least three plants sampled per replicate. Unless otherwise specified, plants were grown on soil as described in Hepworth et al. (2018). Plants were initially grown at 22°C 16hr day/20°C 8hr night for one week ('NV'), before moving to Panasonic MLR-352 series growth cabinets set to 37-52 μmol light (setting 3) for 8 hours per day and the described temperature setting.

For Figures 2 and S4, plants were cycled between cabinets once a week to avoid differences in light quality influencing the experiments. For Figure 2, temperature conditions were: Spike Memory (bright blue), midday spike, 2 hr spike to 21°C, daily 2 hr after dawn, otherwise at 12°C, for 4 weeks, moved to constant 12°C for day of sampling. Night Spike (pink), 2 hr-spike to 21°C every night, 6 hr after dusk, otherwise at 12°C. Midday Spike (green), 2 hr-spike to 21°C every day, 2 hr after dawn, otherwise at 12°C. 12°C constant (dark blue). 14 °C constant (yellow). 14°C fluctuating (red), fluctuating temperature profile as shown in Figure 2A with average temperature of 14.2°C. For Figure S4, temperature conditions were: Night Spike (pink), 2 hr-spike to 21°C every night, 6 hr after dusk, otherwise at 12°C. Evening Spike (purple), 2 hr-spike to 21°C every evening, starting at dusk, otherwise at 12°C. Midday Spike (green), 2 hr-spike to 21°C every day, 2 hr after dawn, otherwise at 12°C. Morning Spike (brown), 2 hr-spike to 21°C every morning, ending at dawn, otherwise at 12°C. 12°C constant (dark blue). 14°C fluctuating (red), fluctuating temperature profile as shown, with average temperature of 14.2°C.

For Figures S9B, S9D, S9E, and S9F (yellow) temperature conditions for vernalization were: constant 5°C, 12°C, 14°C and 22°C respectively.

For Figure S9F (blue) plants were continuously grown at 22°C 16hr day/20°C 8hr night and sampled at the timepoints indicated.

For Figures S9A–S9E (orange and blue) seeds were stratified for 3 days on soil at 5°C. Conditions for vernalization were 2, 4, 8, or 12 weeks at 14°C, 12°C, 8°C (in Panasonic cabinets), 5°C (walk-in vernalization room) or 2°C (Liebherr KP2130 with addition of a controlled lighting system), with low light (~30μmol m^{-2} s^{-1}) and 70% ± ≤10% Relative Humidity.

For Figure S9B (green), plants were grown on petri dishes and experiments were carried out as described in Qüesta et al. (2016).

For Figure S1F, plants were initially grown at 22°C 8hr day/16hr night for the indicated length of time ('No cold' – red) in Panasonic MLR-352 series growth cabinets and then transferred for one day ('+1 day cold' – yellow) to another cabinet of the same make, set to 8°C.

Plant Material for smFISH

Plant root tips were imaged for the smFISH experiments. Plants were sown on petri dishes containing Murashige and Skoog (MS) media minus glucose. They were stratified for 3 days at 5°C and were then grown vertically in growth cabinets at 22°C 16hr day/8hr night for 1 week. Finally, the plants were vernalized at 5°C (walk-in vernalization room), on the vertically oriented petri dishes.

METHOD DETAILS

RNA Preparation and QPCR

RNA extraction and QPCR were used to measure plant average RNA levels (Figures 2, 3, 4, 5, S1F, and S2–S10). Unless otherwise specified, these were performed as described in Hepworth et al. (2018). Gene specific primers used for reverse transcription and primers used for QPCR are listed in Table S1. Samples were normalised to the geometric mean of two standard genes, *PP2A* (At1g13320) and *UBC* (At5g25760). For *FLC* measurements under lab conditions, there was a further normalisation to the 'NV' levels,

sampled before the start of the vernalization treatment. For field experiments (Figures 3, 4, 5, S6, S8F, and S10) and Figure S4 the output was analysed using LinRegPCR (Ruijter et al., 2009). Field experiments 2016-7 were tested for consistency using a new control sample synthesised as in Hepworth et al. (2018).

For Figures S9A–S9E (orange), RNA extraction and QPCR was performed as described in Duncan et al. (2015), using Roche Universal Probe Library (UPL) #65 with primers sFLC_UPL_F and sFLC_UPL_R and expression was normalized to UBC (At5g25760) with primers UBC_UPL_F, UBC_UPL_R and UPL#9 (Table S2).

For Figure S9B (green), samples were normalised to *UBC*.

smFISH

smFISH was used to count *VIN3* mRNA molecules in single cells (Figures S1B–S1E).

Probe Design

We used the online program Stellaris Probe Designer version 2.0 from LGC Biosearch Technologies (California, USA) to design 48 probes complimentary to *VIN3* (At5g57380) exons (see Table S3). Each probe underwent a BLAST assessment to ensure specificity.

Sample Preparation

smFISH was carried out for Arabidopsis roots as described in Duncan and Rosa (2018) and Duncan et al. (2016). Briefly, seedlings were removed from the media and the root tips were cut and fixed in 4% paraformaldehyde for 30 min. The roots were washed twice with nuclease free 1X PBS (Thermo Scientific, Lutterworth, UK) and then placed onto a Poly-L-Lysine slide (Thermo Scientific,) and covered by a glass coverslip (R&L Slaughter, Upminster, UK). The meristems were then squashed under the coverslip, before being submerged in liquid nitrogen until frozen. The coverslips were removed using a razor blade and the roots were left on the slide to dry at room temperature for 30 min. Tissue permeabilization was then carried out by immersing the samples in 70% ethanol for a minimum of one hour.

Probe Hybridization

Following removal from ethanol, slides were left at left room temperature for 5 min before two washes were carried out with wash buffer (10% formamide and 2x saline-sodium citrate buffer; SSC). 100 μL of hybridization solution (10% dextran sulfate, 2x SSC and 10% formamide) containing VIN3 probes (at a final concentration of 250 nM), was added to each slide. Coverslips were placed over the samples to prevent evaporation and the probes were left to hybridize at 37 °C overnight in the dark. Excess hybridization solution (containing unbound probes) was pipetted off the following morning. Each sample was washed twice with wash buffer, with the second wash left to incubate for 30 min at 37°C in the dark. After wash buffer removal, 100 μL of the nuclear stain DAPI (4',6-diamidino-2-phenylindole, 100 ng/ mL) was added to each slide and left to incubate at 37°C for 30 minutes. Following DAPI removal, a 100 μL 2x SSC wash was carried out before 100 μL GLOX buffer (0.4% glucose in 10 mM Tris, 2x SSC) was added to each slide and left to equilibrate at room temperature for 2 min. This was pipetted off and replaced with an anti-fade solution containing 100 μL of GLOX buffer, 1 μL glucose oxidase (#G0543, Sigma) and 1 μL catalase (#C3155, Sigma). The samples were then covered by 22mm x 22mm No.1 coverslips (R&L Slaughter, Upminster, UK), sealed with nail varnish and immediately imaged.

Image Acquisition

For imaging we used a Zeiss Elyra PS1 inverted microscope, with a x100 oil-immersion objective (1.46 NA) and cooled EM-CCD Andor iXon 897 camera (512x512 QE>90%). VIN3 probes were labelled with Quasar570 dye and they were excited using a 561 nm laser and detected at 570-640 nm. For DAPI, an excitation line of 405 nm was used and signal was detected at 420-480 nm.

smFISH RNA Count Quantification

Cellular count quantification of *VIN3* mRNA dots was determined from the z projection of optical sections of cells as described in Duncan et al. (2016). Briefly, we first used Bio-Formats (Linkert et al., 2010) to separate microscopy images into individual channel/z-stack pairs and then implemented the open FISHcount pipeline (available at https://github.com/JIC-CSB/FISHcount) to generate annotated output images showing counts of mRNA per cell. The presence or absence of *VIN3* mRNA within each cell was checked manually using ImageJ (Schneider et al., 2012) or ZEN (proprietary software from Zeiss).

Mathematical Models

Multiple models are presented in this work. Here we first present the ***LCD*** model for *VIN3* and then build on this by describing the ***S*** component that was added to it to create the ***LSCD*** model. We then describe how this was combined with a model for *FLC* to make the *VIN3*/*FLC* model.

LCD *Model*

The rates of change in the concentration of unspliced *VIN3* (*v*) and spliced *VIN3* (*V*) are controlled by the "production" rate (p_v), the splicing rate (s_v) and the degradation rate of the spliced transcript (d_V).

$$\frac{dv}{dt} = p_v(L, C, D) - s_v v$$

$$\frac{dV}{dt} = s_v v - d_V V.$$

The concentration of spliced *VIN3* depends on the concentration of unspliced *VIN3*. In experiments the two show very similar dynamics (Hepworth et al., 2018; Figure 2) and so the degradation rate must be fast. The splicing rate can be estimated in terms of the degradation rate from the ratio of spliced to unspliced *VIN3*. Assuming that the system is at quasi-steady state, $\frac{V}{v} = \frac{s_v}{d_V} \approx 4.4$ (Figure S5A). The good fit of a single straight line to data at various temperatures supports our observation that splicing and degradation of *VIN3* must depend on temperature in the same way, so that the ratio of the rates is not temperature dependent.

Initially, we propose that there are three pathways regulating *VIN3* "production" (p_v): Long-term ($L(T_{his})$), Current ($C(T)$) and Diurnal ($D(t,t_m)$), where T_{his} is the temperature history since sowing, T is the current temperature, t is the time of day and t_m is the time at dawn. For simplicity, we do not treat initiation, elongation and degradation (non-productive transcription) of nascent transcript separately, but combine all three in p_v. The "production" of *VIN3* depends on *L,C,D*, in the form

$$p_v(L, C, D) = L(T_{his})C(T)D(t, t_m).$$

The relationship between *L,C,D* is chosen to be multiplicative, as opposed to additive, because if any of the three is very low, the *VIN3* levels are also very low, regardless of the (obviously bounded) values of the other two. A more complicated relationship between the three pathways may also reproduce our observations, but we chose the simplest form that would be sufficient.

Long-Term Temperature Memory (L)

To allow appropriate accumulation of *VIN3*, *L* must accumulate in the cold and not be strongly affected by temperature fluctuations. As daily maximal *VIN3* levels rise only very slowly in the cold, and moreover *L*'s influence only decays very slowly in the warm (Bond et al., 2009a), *L*'s dynamics must be very slow in all cases. To match these observations, we assume that the degradation/removal of *L*, (d_L), is very slow and temperature insensitive, with *L* only produced/added in the cold ($T<T_L$). Our data supports *L* having a roughly similar response in the range 8 – 14°C (Figure 2D). We therefore use a step function to model *L*, so that there is a single rate of production/addition with value 1 day^{-1} in the cold ($T<T_L$), and value 0 otherwise,

$$\frac{dL}{dt} = \begin{cases} 1 - d_L L, & T < T_L \\ -d_L L, & T \geq T_L \end{cases},$$

where T_L and d_L are parameters defined in the parameter section (Table S4).

Diurnal Regulation (D)

The periodic pattern of transcription of *VIN3* each day (*D*) is given by

$$D = \left[p_D + \sin\left(2\pi\left(t - \frac{t_m - 1}{24}\right)\right)\right]^2,$$

where t_m is the time at dawn, a known input to the model, and p_D is a parameter defined in the parameter section (Table S4). This form was chosen because it always takes positive values and, given certain constraints on the parameters, reproduces the observed narrow peak of transcription (Figures 2, S2, S4, S5B, and S7; Hepworth et al., 2018). We did not attempt to model the circadian clock in a more mechanistic way, as that would require a far more complicated model which lies outside the scope of this work. Instead we simply use a functional form that replicates the observed dynamics.

Current Temperature (C)

The observed *VIN3* levels are different at different temperatures and change quickly in response to temperature changes (Figure 2C). We model this as a temperature dependent change in the *VIN3* transcription rate through the regulator *C*. We found that *L* responds in a roughly similar way for all temperatures tested up to 14°C (Figure 2D). Therefore, after the same cold exposure (same *L*), and at the same time of day (same *D*), any remaining differences must be due to *C*. We looked at data sampled between 14:30 and 17:30 after 4 weeks at different constant temperatures (Figure S5C) to determine an appropriate functional form of the temperature sensitivity of *C*. We used a piecewise linear function of the form

$$C(T) = \begin{cases} p_{C1}, & T \leq T_{C1} \\ c(T), & T_{C1} < T < T_{C2} \\ p_{C1} - p_{C2}, & T \geq T_{C2} \end{cases},$$

where

$$c(T) = p_{C1} - \frac{T - T_{C1}}{T_{C2} - T_{C1}} p_{C2},$$

and T_{C1}, T_{C2}, p_{C1}, p_{C2} are parameters defined in the parameter section (Table S4).

LSCD Model

From the work presented in Figure 2, we found that a further pathway that regulates transcription of *VIN3* in response to temperature needed to be added to the ***LCD*** model. We termed this the Short-term memory ($S(T_{max})$, where T_{max} is defined below) and developed

the ***LSCD*** model. The equations for *v, V, L, C, D* are the same in this model as in the ***LCD*** model, with the only difference being that the "production" rate of *VIN3* now becomes

$$p_v(L,S,C,D) = L(T_{his})S(T_{max})C(T)D(t,t_m).$$

Short-Term Memory (S)

We observed that a spike to high temperature regulated *VIN3* immediately through *C*, but also decreased the levels of *VIN3* over a longer but limited time window. Here we used a purely phenomenological approach with the simplest form, a step function, with a high value for no spike to high temperature, and a lower value if there was such a spike since the previous evening. Our assumption is that this short-term memory is wiped (actively forgotten) every evening. Indeed, in Figures 2B and 2C, at the 18:30 timepoint, just after the lights are turned off, the levels of treatments with a temperature spike appear to be "reset" to the levels of the treatments with the constant background temperature. We take ***S*** to have the explicit form

$$S = \begin{cases} 1, & T_{max} < T_{\boldsymbol{S}} \\ S_1, & T_{max} \geq T_{\boldsymbol{S}} \end{cases},$$

where T_{max} is the maximum temperature since the last resetting, which was chosen to occur each day at 4pm. T_S and S_1 are parameters defined in the parameter section (Table S4).

We now examine whether the addition of ***S*** might permit the removal of ***C*** from the model. We have already observed that in response to cold we see an immediate response (Figure 2C). We can further see a partial recovery from the effect of the warm spike upon return to cool temperatures in the spike treatments (Figures 2B and 2C). Conversely, if the warm period persists, as it does in the post-cold experiment of Figure S2B (data from Hepworth et al., 2018), the *VIN3* levels do not recover. In both these treatments ***S*** is triggered, while ***L*** and ***D*** are similar, yet different *VIN3* levels are observed. Therefore, thermosensors ***S*** and ***C*** are both required.

FLC Model

The principle behind this model is that vernalization is controlled by a sequence of cell-autonomous switches between digital states: ***H*** (**H**igh transcription), ***I*** (**I**nactive) and ***E*** (**E**pigenetically silenced). Switches between these states involve the VIN3-independent pathway (***H*** ↔ ***I*** switch) and the VIN3-dependent pathway (principally the ***I*** → ***E*** switch, but also the weaker ***H*** → ***E*** switch), and may be controlled by temperature directly or indirectly though the concentration of regulatory factors. The fraction of gene copies in each of these states is represented by the variables *H*, *I* and *E* in the model, respectively, so that $H + I + E = 1$. Ordinary differential equations were used to describe the dynamics of *H*, *I* and *E*, and take the form

$$\frac{dH}{dt} = -s_1 H + r(T_n)I - s_3(V,T)H$$

$$\frac{dI}{dt} = s_1 H - r(T_n)I - s_2(V,T)I$$

$$\frac{dE}{dt} = s_2(V,T)I + s_3(V,T)H,$$

where s_1, $r(T_n)$, $s_2(V,T)$, $s_3(V,T)$ determine the rates of the transitions and are explained in detail in the following sections.

VIN3-Independent Pathway

In the VIN3-independent pathway, we found that it is necessary for at least the ***I*** to ***H*** transition (*r*, Figures 4A and 4B) to be temperature regulated. Examining the data for the *vin3-4* mutant (Yang et al., 2017), we see that *FLC* decreases slowly in the cold over many weeks, but reactivates at a much higher rate in the warm. This must mean that *H* also decreases slowly in the cold and increases rapidly in the warm. For *vin3-4*, there is no VIN3 protein and therefore the ***I*** to ***E*** and ***H*** to ***E*** transitions are blocked ($s_2 = 0$, $s_3 = 0$). Consequently, the epigenetically silenced state ***E*** cannot be reached in this mutant ($E = 0$ at all times) and so only two states exist, ***I*** and ***H***. Because the variables (*H,I,E*) are defined as fractions, we can replace $I = 1 - H$, and so the equation for *H* becomes

$$\frac{dH}{dt} = r - (r + s_1)H.$$

If *r* is not temperature sensitive, and because any increase in *H* is limited by this parameter, *r* must take a high value to permit the rapid increase in the warm. In that case, regardless of the value or temperature sensitivity of s_1, it is impossible to have slow dynamics in the cold. Therefore, we conclude that *r* must be temperature sensitive. A low value of *r* in the cold could reflect the presence of antisense *COOLAIR* foci, impeding the return to a high *FLC* sense transcription state (Rosa et al., 2016). It is of course possible that s_1 is also affected by temperature but, as we attempt to minimise the number of processes controlled by temperature to only those where it is strictly required, we assume here that s_1 is temperature independent.

We further found that the VIN3-independent pathway is sensitive to night-time temperatures (T_n). Night-time is defined as the time from 6 hr before midnight to 6 hr after midnight. The duration of this time range was selected to approximately match the average

night temperature in the night spike experiment with 14°C, the constant temperature that gives similar downregulation of *FLC* (Figure 2E). The experiment of Figure S4 further supports this assumption, since the morning and evening spikes, which were during the dark but outside of the 12 hrs of "night-time" did not significantly decrease the rate of shutdown due to the VIN3-independent pathway. For simplicity we used a piecewise linear function for the temperature sensitivity of $r(T_n)$,

$$r(T_n) = \begin{cases} 0, & T_n \le T_{r1} \\ p_r \dfrac{T_n - T_{r1}}{T_{r2} - T_{r1}}, & T_{r1} < T_n < T_{r2} \\ p_r, & T_n \ge T_{r2} \end{cases},$$

where T_{r1}, T_{r2} and p_r are parameters defined in the parameter section (Table S4).

VIN3-Dependent Pathway

For the VIN3-dependent transitions to the ***E*** state (***I*** to ***E*** and ***H*** to ***E***), we assumed that the rates of the transitions $(s_2,\ s_3)$ depend on the concentration of VIN3 protein, which we approximated with our predicted *VIN3* mRNA levels since we know that, at least in the warm, the protein dynamics are fast (Yang et al., 2017). Indeed, in the absence of *VIN3*, epigenetic silencing does not occur (Sung and Amasino, 2004), or occurs only very slowly (Buzas et al., 2011). Additionally, in constant conditions, the fraction of epigenetically silenced *FLC* copies increases slowly at first, before accelerating (Angel et al., 2015). Both of these cases are consistent with increasing *VIN3* levels affecting the rates of these transitions.

The rates $s_2,\ s_3$ were also assumed to depend directly on temperature. It has been reported that, in the warm, overexpression of *VIN3* does not lead to epigenetic silencing of *FLC* (Kim and Sung, 2017; Lee et al., 2015). Additionally, at temperatures close to 0°C, vernalization was found to be less effective (Duncan et al., 2015; Napp-Zinn, 1957; Wilczek et al., 2009). In field experiments, the slope of the *FLC* shutdown was anticorrelated with mean temperature at the three sites (Figure S5D; data from Hepworth et al., 2018), meaning higher temperatures gave a faster rate of shutdown, despite similar *VIN3* levels (Figure S5E; data from Hepworth et al., 2018). Therefore, we take the epigenetic silencing rate (***I*** to ***E*** switch) to be of the form

$$s_2(V,T) = \begin{cases} p_s V\,(T - T_1)(T_2 - T), & T_1 < T < T_2 \\ 0, & T \le T_1 \text{ or } T \ge T_2 \end{cases},$$

where T is temperature, V is the *VIN3* concentration and $T_1,\ T_2,\ p_s$ are parameters defined in the parameter section (Table S4), thus reflecting the absence of epigenetic silencing at high or very low temperatures (Figure S5F).

We also allow for a direct transition from ***H*** to ***E*** (s_3) in the absence of the VIN3-independent pathway. For this direct transition, we choose a lower maximum rate but the same form as for s_2 in terms of the temperature and *VIN3* concentration,

$$s_3(V,T) = p_{s3} s_2(V,T),$$

where p_{s3} is a parameter defined in the parameter section (Table S4).

This transition gives the acceleration of silencing observed in the later timepoints in Norwich 2014-15 after *VIN3* upregulation (Figures 3C and 4C), and explains the difference in *FLC* shutdown rate between the *vin3-4* mutant and Col*FRI*^{SF2} plants at low temperatures (Figures S8 and S9).

FLC mRNA Dynamics in the Model

FLC is transcribed only in the ***H*** state of the *FLC* gene. We modelled the normalised *FLC* mRNA concentration, [*FLC*], using the form

$$\frac{d[FLC]}{dt} = p_f \left(\frac{H}{H_0} - [FLC] \right),$$

where H_0 is the initial condition of H and p_f is a parameter defined in the parameter section (Table S4).

Initial Conditions and Numerical Simulation

The initial conditions of our system were chosen such that the system is at steady state in the warm, with the normalised *FLC* mRNA concentration, [*FLC*], equal to 1. Therefore, at $t = 0$,

$$H = H_0 = \frac{p_r}{s_1 + p_r}$$

$$I = \frac{s_1}{s_1 + p_r}$$

$$E = 0$$

$$[FLC] = 1,$$

for the *FLC* model and

$$B = 0$$

$$v = 0$$

$$V = 0,$$

for the ***LSCD*** model.

Matlab version R2016a was used to solve the models numerically with solver ode15s (Shampine and Reichelt, 1997).

Parameters

The parameter values used for the ***LCD*** model in Figure S2 are given in the figure legend. In all other cases, the parameters used are shown in Table S4.

Temperature Modifications

To test the effect of different features of the temperature profile on the model, we modified the measured temperature profiles and predicted *VIN3* and *FLC* levels with these new modified profiles. These profiles were:

Day-mean (Figure S11A): The average temperature for each day (midnight to midnight) was calculated and the temperature between midnight and 0.01 days (~15min) before the next midnight was set to this average value. Outside those times (in the transition time between days), linear interpolation was used to determine the temperature.

+3 (Figures S11B and S11D): We added 3°C to each temperature measurement in the entire field temperature profile, with the exception of temperatures below 0.5°C and above -0.5°C, when the plants and the temperature loggers were often covered by snow and so our measurements were not reflecting the air temperature. Only temperatures in Sweden were affected by this exception. Since we do not have measurements for the air temperature at that time, we made the conservative assumption that the snow cover will not be affected by warming. Without this assumption, the temperatures in Sweden would rise for long periods from 0°C to 3°C. This change would not affect *VIN3* expression but would increase s_2 and s_3 due to their temperature sensitivity.

x2 (Figures S11C and S11E): For each day (midnight to midnight) we calculated the daily mean temperature (T_m), and stretched the field temperature profile T above and below this value, so that the mean temperature over that 24 hr was not changed. For each measurement, we replaced the temperature T with a stretched value (T_{x2}), where

$$T_{x2} = 2(T - T_m) + T_m.$$

QUANTIFICATION AND STATISTICAL ANALYSIS

All replicate numbers are reported in the supplementary table file and figure legends.

Experimental Data Comparison

For Figures 2E, S4E, and S4F, the non-parametric Kruskal-Wallis test with Dunn's post-hoc test was performed on *FLC* expression values to test for the effect on the VIN3-independent pathway, by testing conditions with similar *VIN3* levels (i.e., all the spike and spike-memory treatments) using GraphPad Prism version 5.04 for Windows, GraphPad Software, San Diego, California, USA, www.graphpad.com.

Mathematical Model Optimisation

The model was optimised in parts as shown in Table S4: the ***LSCD*** model was compared to *VIN3* experimental data (parameters d_V, S_1, T_L, d_L, T_{C1}, T_{C2}, p_{C1}, p_{C2}, p_D), the VIN3-independent switch of the *FLC* model was compared to *vin3-4* , *vrn2-1* and *vrn5-8* mutant *FLC* experimental data (parameters s_1, T_{r1}, T_{r2}, p_r, p_f) and the VIN3-dependent switch was optimised last and compared to the *FLC* experimental data for the wild-type Col*FRI*^{SF2} (parameters T_1, T_2, p_s, p_{s3}), using the values from the two previous optimisation results for the other parameters. This separation was natural in terms of the variables and conditions being compared and it also allowed us to optimise only a few parameters at any time (no more than 10). For each group of parameters, there is a large set of experimental data used to constrain them (***LSCD***: 999 measurements, VIN3-independent *FLC*: 478 measurements, VIN3-dependent *FLC*: 1574 measurements).

For the ***LSCD*** model, each of the components could initially be fit separately, by using combinations of data that differed in only one of ***L***, ***S***, ***C*** or ***D***, thus further reducing the number of parameters that were fit together. Optimisation was then performed manually in the first instance, by visual comparison of the data to the model predictions ("fitted" data plots in Figures 3, 4, S6, S7, S8, and S9), in order to capture primarily the "qualitative features" of the data, as described below. The parameters obtained in this way already showed a good fit to the data.

We then moved to an automated optimisation method, using the SciPy basin-hopping algorithm in Python (Jones et al., 2001; Wales and Doye, 1997). For the local minimisation, the Nelder-Mead method was used with a maximum allowed number of iterations

of 10. The number of basin hopping iterations was 200 and a random displacement of the coordinates (sampled from a uniform distribution $U(-stepsize, stepsize)$) was used for the step taking routine with an initial step size (take_step.stepsize) of 0.05. At every step, the parameter bounds were applied, as shown in Table S4.

To evaluate the model *FLC* and *VIN3* levels for comparison to the experimental data, we used the Scipy odeint solver (Jones et al., 2001). Two cost functions were minimised in separate runs of the algorithm. The first was the sum of squared errors (*SSE*)

$$SSE = \sum_i (y_i - f(x_i))^2,$$

where y_i are the data and $f(x_i)$ are the corresponding model predictions. The second cost function additionally included the fold-differences, to improve the fit to small values of the data:

$$SSE_{\log} = \sum_i \left((y_i - f(x_i))^2 + (\log(y_i) - \log(f(x_i)))^2 \right).$$

Both cost functions were tested for the optimisation of the ***LSCD*** model parameters, while only the second was used for the *FLC* model, where fold-differences are more important, especially at later times.

Automated optimisation allowed us to explore the parameter space more fully. The optima obtained by the optimisation algorithm were compared visually to the data and to the manually fitted model. Again, priority was given to capturing qualitative features (listed below), which the automated optimisation could not test.

In the case of the ***LSCD*** model and the VIN3-dependent part of the *FLC* model, only the manually selected parameters could capture all the qualitative features. In the automatic optimisation, to achieve a lower value of the cost function, it was often "optimal" to ignore some data points and improve the fit of the majority. However, in some cases, such as the Spike conditions, single data points gave important qualitative behaviour that was lost in the "optimised" fit. It was not possible to develop an appropriate cost function to avoid such losses, due to the large number and complexity of the qualitative features that we wanted to reproduce in these models. For this reason, the manually optimised parameters were finally used in further work for the ***LSCD*** and VIN3-dependent *FLC* models. On the contrary, in the case of the VIN3-independent part of the *FLC* model, the qualitative features were simpler and could be captured by the cost function. Therefore, the automated optimisation allowed an improvement of the qualitative fit in that case.

The parameter values that were chosen manually, and the improved parameter set after the automatic optimisation, were both tested against the new data and successfully captured the observed behaviour. This success satisfied the intended purpose of the modelling, which was to show that the structure of the model could reproduce and predict *FLC* dynamics, thus supporting our underlying mechanism.

"Qualitative features" for the ***LSCD*** model:

1. Slow increase of *VIN3* over weeks in the cold (Figure S7B).
2. Lower levels of *VIN3* for higher constant cold temperatures above 8°C (Figures S7B, S7E, and S7F).
3. Very low levels of *VIN3* in the warm and, in particular, for unspliced *VIN3* immediately during a warm temperature spike (Figures S7A, S7E, and S7F).
4. Diurnal pattern of *VIN3* with low levels in the morning and night, and peak levels in the afternoon (Figures S7C–S7F).
5. Similar *VIN3* levels between 8°C fluctuating and 8°C constant, but different levels between 14°C fluctuating and 14°C constant (Figures S7C and S7D).
6. Similar *VIN3* levels between Midday spike and Night spike, and similar *VIN3* levels between Spike memory and 12°C constant (Figures 2, S3, S4, S7E, and S7F).
7. Low *VIN3* levels early in Norwich 2014-15, and rapid increase to high levels at approximately 55 days (Figure 3C).

"Qualitative features" for the *FLC* model

1. VIN3-independent (comparing with the *vin3-4, vrn2-1, vrn5-8* mutants)

a.Different rate of *FLC* downregulation at different temperatures (Figure S8).
b.Slow rate of shutdown over many weeks in the cold (Figure S8).
c.Faster rate of reactivation over ~10 days in the warm (grey in Figures S8A and S8F).
d.Decrease in the rate of *FLC* downregulation in the case of night spikes but not Midday spikes (Figures 2 and S4).

2. VIN3-dependent (using previously determined parameters for the VIN3-independent part and ***LSCD*** model, and now comparing with Col*FRI*^{SF2} data)

a.Different rate of *FLC* downregulation at different temperatures, faster than for the *vin3-4* mutant (Figure S9).
b.Different rates of *FLC* downregulation at different field sites (Figures 4C, 4D, 4E, S5D, S6B) and in particular for Norwich, different rates before/after *VIN3* induction (~55 days) (Figure 4C).
c.No reactivation in post-cold warm conditions (Hepworth et al., 2018; Sung and Amasino, 2004).
d.No decrease of *FLC* in the warm (Figure S9F).

Model Sensitivity to the Long-Term Timescale

An approximate 20% change in the timescale of ***L*** was implemented using the parameter d_L, by adding or subtracting 20% from its central value, and calculating the system sensitivities *SSE* and SSE_{log} in both cases. For all other parameters, the values from Table S4 were used. The relative change in *SSE* was calculated as shown:

$$\frac{\Delta SSE_{+}}{SSE(d_L)} = \frac{|SSE(1.2d_L) - SSE(d_L)|}{SSE(d_L)} = 0.0419,$$

$$\frac{\Delta SSE_{-}}{SSE(d_L)} = \frac{|SSE(0.8d_L) - SSE(d_L)|}{SSE(d_L)} = 0.0185,$$

$$\frac{\Delta SSE_{log+}}{SSE_{log}(d_L)} = \frac{|SSE_{log}(1.2d_L) - SSE_{log}(d_L)|}{SSE_{log}(d_L)} = 0.0074,$$

$$\frac{\Delta SSE_{log-}}{SSE_{log}(d_L)} = \frac{|SSE_{log}(0.8d_L) - SSE_{log}(d_L)|}{SSE_{log}(d_L)} = 0.0038.$$

VIN3 Model Comparison Using AIC

Akaike's information criterion (AIC) was calculated for the two models (***LCD*** and ***LSCD***) based on the new data of Figure 2B (conditions: 12°C constant, Midday Spike, Night Spike, Spike Memory; 134 observations). The two models were first fit to this data alone, using the automated fitting algorithm described above with the *SSE* cost function, in order to give them an equal footing against this dataset. They were subsequently compared visually against the same experimental data and the improved fit of the new parameters was confirmed also in relation to capturing the qualitative features present in this dataset. The parameter values that optimised the two models are shown in Table S5. The number of parameters, including the variance, was 10 and 12 for the ***LCD*** and ***LSCD*** models, respectively.

The Common Formulation

$$AIC = 2k + n\ ln(SSE),$$

was used, where *k* is the number of parameters (including a parameter for the variance of the residuals), *n* is the number of the observations and *SSE* is defined previously. In this formulation, we ignore the constant terms that will cancel out in the model comparison. The relative likelihood of the models was calculated using

$$e^{\frac{AIC_{min} - AIC_{model}}{2}}.$$

The ***LSCD*** model had the minimum AIC and the relative likelihood of the ***LCD*** model was 5×10^{-7}, meaning the ***LCD*** model is 5×10^{-7} times as probable as the ***LSCD***, based on the AIC. Based on this analysis, we can confidently reject the ***LCD*** model.

DATA AND SOFTWARE AVAILABILITY

Microscopy images for VIN3 RNA smFISH (Figures S1B–S1E) are available from figshare. https://doi.org/10.6084/m9.figshare.7346552.